# Massive quantum superpositions using magnetomechanics

Sarath Raman Nair,[1,2,*,†] Shilu Tian,[3,*,‡] Gavin K. Brennen,[1,2] Sougato Bose,[4] and Jason Twamley[3]

[1] *School of Mathematical and Physical Sciences, Macquarie University, Sydney, NSW 2109, Australia*

[2] *ARC Centre of Excellence for Engineered Quantum Systems (EQUS), Macquarie University, Sydney, NSW 2109, Australia*

[3] *Quantum Machines Unit, Okinawa Institute of Science and Technology Graduate University, Onna, Okinawa, 904-0495, Japan*

[4] *Department of Physics and Astronomy, University College London, Gower Street, WC1E 6BT, London, United Kingdom*

(Received 20 July 2023; revised 19 June 2025; accepted 20 June 2025; published 26 August 2025)

Macroscopic quantum superpositions of massive objects are very interesting as they have several potential applications, ranging from the exploration of the interaction of gravity with quantum mechanics to quantum sensing. In this article, we propose two related schemes to prepare a spatial superposition of massive quantum oscillator systems with a high $Q$ factor via a superposition of magnetic forces. In the first method, we propose a large spatial superposition of a levitated spherical magnet generated via magnetic forces applied by adjacent flux qubits. We find that in this method the spatial superposition extent $\Delta z$ is independent of the size of the particle. In the second method, we propose a large spatial superposition of a magnetically levitated flux qubit, generated via our driving the levitated qubit inductively. In both schemes, we show that ultralarge superpositions $\Delta z/\delta z_{\mathrm{ZPM}} \sim 10^4$–$10^6$ are possible, where $\delta z_{\mathrm{ZPM}}$ is the zero-point motional extent.

DOI: 10.1103/scnr-2rkt

## I. INTRODUCTION

The generation of macroscopic quantum superpositions of coherent states, sometimes known as Schrödinger cat states [1], is one of the most-sought-after goals in quantum mechanics. Such superpositions can be used to probe the domain of validity of quantum mechanics, whether gravity can entangle objects (i.e., quantum gravity–induced entanglement of masses), and the validity of various collapse models [2–6], and for extremely high precision sensing [7]. By preparing multiple macroscopic quantum superposition states, one can test the ability of space-time itself to exist in a quantum superposition state [8–11], and this topic has attracted much attention and discussion recently [11–21]. It would be highly desirable to make Schrodinger cats that have both large mass and large spatial extent as such states would be more useful for the above-mentioned applications.

Although there are many proposals for the generation of spatial superpositions of the center of mass of a massive object, they are all, in one way or the other, highly technically challenging. These proposals include the use of supramolecular complexes [22,23], optomechanical systems [24–38], magnetomechanical systems [9,39–43], and cold atomic systems [44,45]. Furthermore, the experimental demonstration of a macroscopic superposition of the bulk acoustic mode of matter with effective mass $M \sim 16\ \mu$g [46] has been shown toward this end.

In this study, we propose two complementary schemes that have the potential to generate ultralarge spatial superpositions for massive objects, based on the magnetic forces exerted by superconducting (SC) flux qubits. Briefly, the first scheme involves a levitated magnetic sphere with fixed flux qubits situated near it, and the second scheme involves an isolated floating flux qubit levitated by a fixed magnetic sphere. These proposals enable the extra-large spatial superpositions, which are not limited by the size of the objects.

## II. MODEL

We first describe both our schemes in a general theoretical framework by considering a levitated spherical magnet or a levitated flux qubit. We assume a coordinate system with the origin at the equilibrium position of this oscillator

*Joint first authors.

†Contact author: sarath.raman-nair@mq.edu.au

‡Contact author: shilu.tian@oist.jp

*Published by the American Physical Society under the terms of the Creative Commons Attribution 4.0 International license. Further distribution of this work must maintain attribution to the author(s) and the published article's title, journal citation, and DOI.*

and consider that an external magnetic actuation to create the superposition state is present along the $z$ axis. We denote the mass of the oscillator as $M$ and the oscillation frequency along the $z$ axis as $\omega_z$. We consider that the oscillator is in its motional ground state with a ground state width denoted as $\delta z_{\mathrm{ZPM}} = \sqrt{\hbar/2M\omega_z}$, where $\hbar$ is the reduced Planck constant [39,47]

For the creation of superposition states, we consider logical states $|0\rangle$ and $|1\rangle$ based on superconducting flux qubits. The superconducting flux qubit allows only integer numbers of the magnetic flux quantum ($\Phi_0 = 2.068 \times 10^{-15}$ Wb) threading the qubit loop, and the flux qubit will generate a supercurrent to compensate for any noninteger flux quanta threading through its loop. Since logical states of flux qubits are determined by the direction of large circulating persistent currents in the superconducting flux qubit (currents flow either clockwise or counterclockwise) [47,48], the flux qubit can generate logical state-dependent magnetic forces.

We denote the logical state-dependent magnetic forces generated by the flux qubit as $\vec{F}_{\mathrm{FQ}}^{|q\rangle}$ for the rest of this article, and we assume that they are along the $z$ axis, where $|q\rangle$ is the logical state. $\vec{F}_{\mathrm{FQ}}^{|0\rangle}$ ($\vec{F}_{\mathrm{FQ}}^{|1\rangle}$) is considered to be along the positive (negative) $z$ axis, displacing the equilibrium position of the oscillator away from $z = 0$ to the new position $z = z_{\mathrm{eq}}$ ($z = -z_{\mathrm{eq}}$). However, a restoring force $\vec{F}_{\mathrm{tr}} = -M\omega_z^2\vec{z}$ due to the trapping of the oscillator along the $z$ axis acts on the displaced oscillator and pulls it back from the positive and negative $z$ axis directions toward $z = 0$. As a result, the oscillator reaches a new equilibrium position where $\vec{F}_{\mathrm{FQ}}^{|q\rangle} + \vec{F}_{\mathrm{tr}} = 0$. When a superposition state $\frac{1}{\sqrt{2}}(|0\rangle + |1\rangle)$ is created with the use of a flux qubit state (or the state of multiple flux qubits depending on the scheme), the oscillator is pushed to a macroscopic spatial superposition of spatial extent $\Delta z = 2z_{\mathrm{eq}}$. We express the spatial extent in terms of a dimensionless factor $\chi$ defined as $\chi = \Delta z/\delta z_{\mathrm{ZPM}}$.

We now consider both schemes to estimate $\vec{F}_{\mathrm{FQ}}^{|q\rangle}$ and thereby estimate $\chi$ for each case. In both schemes, we model the uniformly magnetized spherical magnets as magnetic dipoles. We model flux qubits as superconducting rings with radius $R$ and denote the modulus of the supercurrent as $|I|$. We consider a flux qubit with loop radius $R = 183$ μm and cross-section radius $a = 5$ μm, with self-inductance $L = 0.85$ nH, For a one-flux-quantum jump the current jumps by $\Phi_0/L = 2.4$ μA, and for simplicity we choose $I = \pm 1$ μA. The size of this flux qubit ring is designed to ensure stable trapping, as discussed later.

### A. Motional superposition of a levitated spherical magnet

We focus first on our scheme to generate a macroscopic superposition of a levitated magnet under the influence of a superposition of forces generated by nearby fixed flux qubits. We consider a levitated spherical magnet [for example, an vttrium iron garnet (YIG) magnetic microparticle] with magnetic moment denoted as $\vec{m}_0$. The YIG sphere can be magnetically levitated above a superconducting block with a rectangular hole (see Appendix A for more details).

We consider the levitated YIG sphere with the primary trapping axis to be along the $x$ axis (axes depicted in Fig. 1) and the trapping force is strongest along the $x$ axis compared with the $y$ and $z$ axes. Two entangled flux qubits with identical supercurrents flowing with opposite helicity are placed coaxial along the $z$ axis symmetrically on either side of the trapped spherical magnet, as shown in Fig. 1. The supercurrents generate magnetic fields emanating from the flux qubits in an anti-Helmholtz configuration. When each qubit is in the $|0\rangle$ ($|1\rangle$) state, $B_z(z)$ at the midpoint between the two flux qubits vanishes and varies linearly around there, i.e., $B_z(z) \propto z$ [$B_z(z) \propto -z$]. Because of the combination of a vanishing magnetic field and a nonvanishing gradient at the YIG's central location, only translational motion is excited. We assume that any change in the magnetic field produced by this YIG at the locations of the flux qubit due to the movement of the YIG within the trap is negligible or compensated appropriately in the experimental implementation (see Appendix B for estimates). For this scheme, $F_{\mathrm{FQ}}^{|q\rangle} = \vec{m}_0 \cdot (\partial\vec{B}_z/\partial z)_{|q\rangle}$.

We model the two flux qubits as superconducting rings. For this we assume that these rings have radii $R$, and each

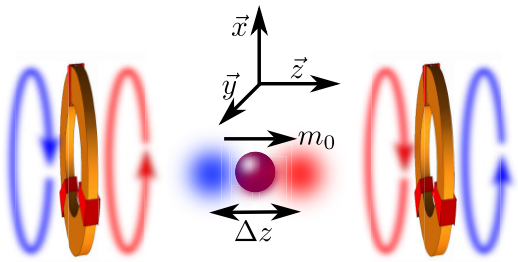



FIG. 1. Creation of superposition states of a levitated magnetic YIG microparticle (oscillator) using superconducting flux qubits (not to scale). We depict the oscillator as a sphere that is trapped at the center. The nearby flux qubits are shown as rings (orange), containing three Josephson junctions. The two flux qubits are connected in the entangled state to ensure that the supercurrent in each qubit has the same magnitude but opposite circulating directions to excite only translational motion. When both qubits are in the $|0\rangle$ ($|1\rangle$) state, current flows in opposite circulating directions depicted in blurred red (blue) ring arrows, and the corresponding magnetic field is in the anti-Helmholz configuration. Then the entangled qubit state $|0\rangle|0\rangle$ ($|1\rangle|1\rangle$) shifts the spherical magnet to the right (left) by a small distance $z_{\mathrm{eq}}$ as shown by the blurred red (blue) sphere. By excitation of the flux qubits into a superposition state $\sim (|0\rangle|0\rangle + |1\rangle|1\rangle)$, the microparticle is driven into a spatial superposition of extent $\Delta z = 2z_{\mathrm{eq}}$.

of these flux qubits is symmetrically located at a distance $z_{\pm}^{\mathrm{FQ}} = \pm\eta R$ along the $z$ axis around the origin, where $\eta$ is a dimensionless scaling factor. The flux qubits have supercurrents $I$ circulating in each ring. We can write down the magnetic field generated by the two superconducting flux qubits at a point on the $z$ axis $\vec{r} = (0, 0, \vec{z})$ as

$$B_z(z)_{|q\rangle} = (-1)^q \times \frac{\mu_0 |I| R^2}{2} \times \left[\frac{1}{((z-\eta R)^2 + R^2)^{3/2}} - \frac{1}{((z+\eta R)^2 + R^2)^{3/2}}\right], \tag{1}$$

where $\mu_0$ is the vacuum permeability. The gradient of the magnetic field can be obtained as

$$\left(\frac{\partial B_z}{\partial z}\right)_{|q\rangle} = (-1)^q \times \frac{3\mu_0 |I| R^2}{2} \left[-\frac{(z-\eta R)}{((z-\eta R)^2 + R^2)^{5/2}} + \frac{(z+\eta R)}{((z+\eta R)^2 + R^2)^{5/2}}\right]. \tag{2}$$

Around the origin ($z \to 0$) the magnetic field gradient is given by

$$\left(\frac{\partial B_z}{\partial z}\right)_{|q\rangle} = (-1)^q \frac{3\mu_0 |I|}{R^2} \frac{\eta}{(1+\eta^2)^{5/2}}, \tag{3}$$

which can be approximated to be constant.

We find that for fixed $|I|$ and $R$, $(\partial \vec{B}_z/\partial z)_{|q\rangle}$ at the origin is maximum when $\eta = 0.5$; that is, each of the flux qubits is symmetrically located at a distance $z_{\pm}^{\mathrm{FQ}} = \pm R/2$ along the $z$ axis around the origin. Thus, we consider this as the location of the flux qubits for the present scheme.

We consider $\vec{m}_0$ to be along the positive $z$ axis (similarly to the experimental study reported in Ref. [49]). We can write $|\vec{m}_0| = \mu_0^{-1} B_{\mathrm{r}} V$, where $B_{\mathrm{r}}$ is the remanent magnetic field. The new equilibrium position $\pm z_{\mathrm{eq}}$ can be found by one balancing the actuation force from the flux qubits and the restoring trapping force to find

$$\frac{B_{\mathrm{r}}}{\mu_0} V \left(\frac{\partial B_z}{\partial z}\right)_{|q\rangle} - \rho V \omega_z^2 z_{\mathrm{eq}} = 0. \tag{4}$$

Using Eq. (2) to express the field gradient, we can write Eq. (4) as

$$\frac{3(-1)^q |I| B_{\mathrm{r}} R^2}{\rho \omega_z^2} \left[\frac{(z_{\mathrm{eq}} - (R/2))}{((z_{\mathrm{eq}} - (R/2))^2 + R^2)^{5/2}} - \frac{(z_{\mathrm{eq}} + (R/2))}{((z_{\mathrm{eq}} + (R/2))^2 + R^2)^{5/2}}\right] + z_{\mathrm{eq}} = 0, \tag{5}$$

where we considered $\eta = 1/2$. Then for the superposition of $|0\rangle$ and $|1\rangle$, we can obtain the spatial superpostion extent as $\Delta z = 2z_{\mathrm{eq}}$. We can write Eq. (5) using the transformation $z_{\mathrm{eq}} \to (\Delta z/2)$ to obtain an equation in terms of $\Delta z$ for numerical calculations as

$$\frac{3|I| B_{\mathrm{r}} R^2}{\rho \omega_z^2} \left[\frac{((\Delta z/2) - (R/2))}{((\Delta z/2) - (R/2))^2 + R^2)^{5/2}} - \frac{((\Delta z/2) + (R/2))}{((\Delta z/2) + (R/2))^2 + R^2)^{5/2}}\right] + (\Delta z/2) = 0. \tag{6}$$

From Eq. (6), we can see that $\Delta z$ is independent of the size of the magnetic sphere but depends only on $\rho$ and $B_{\mathrm{r}}$.

We numerically study the extent of the spatial superposition $\Delta z$ of the YIG sphere as a function of the radius of the flux qubits on the basis of Eq. (6) (see Table I in Appendix F for numerical values of the parameters used); the results are shown in Fig. 2. We consider a YIG sphere of radius 25 μm, which is similar in size to other micromagnets that have been levitated experimentally in magnetic traps [49–51]. For the present scheme, $\Delta z$ can be on the order of hundreds of nanometers and $\chi$ can be on the order of $10^6$.

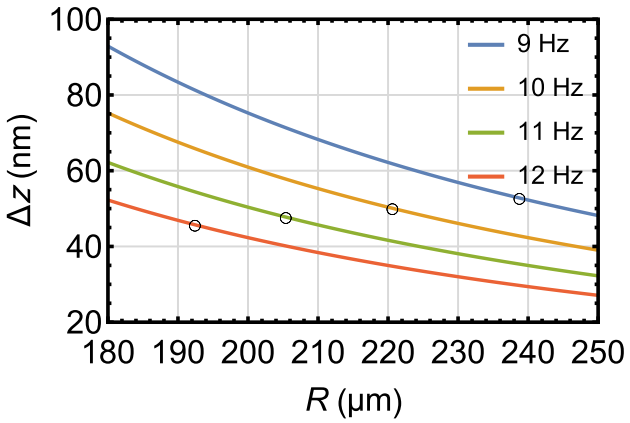



FIG. 2. Numerical analyses of spatial superposition separation $\Delta z$ as a function of the radius $R$ of the flux qubit for trapping frequency $\omega_z/2\pi$ as shown in the legends, based on Eq. (6). The open circles on each curve show where $\chi = 10^6$ for a YIG sphere with a radius of 25 μm.

### B. Motional superposition of a trapped superconducting flux qubit

We now describe a complementary scheme to generate a macroscopic spatial superposition by levitating an entire superconducting flux qubit ring above a small fixed magnet. The flux qubit contains persistent circulating currents that generate large magnetic moments that, when interacting with the magnetic field produced by the magnet, shift the levitation height of the flux qubit. These circulating currents can be controlled and put into a superposition by inductive driving of the qubit. By driving of the qubit into a superposition of circulating currents, the qubit is forced into a superposition of heights.

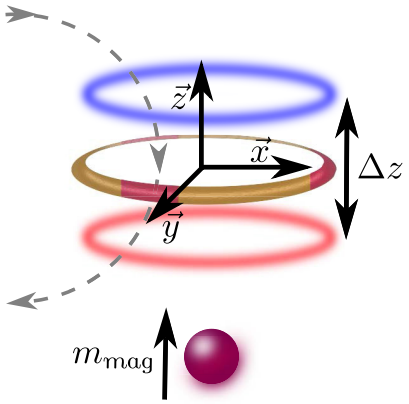



FIG. 3. Creation of macroscopic superposition using the levitated superconducting flux qubit (not to scale). The superconducting flux qubit is stably levitated above a magnetic dipole (practically a spherical micromagnet) due to flux-threading conservation and superdiamagnetism. The levitated flux qubit is driven inductively with the use of a nearby superconducting circuit. The dashed gray line represents an induced magnetic flux line. The levitated flux qubit in the $|0\rangle$ ( $|1\rangle$) state is displaced upward (downward) as depicted by the blue (red) ring. By creation of a superposition state of $|0\rangle$ and $|1\rangle$ states, the levitated flux qubit is driven into a spatial superposition of extent $\Delta z = 2z_{\mathrm{eq}}$.

We consider the flux qubit (in the shape of a ring) to be magnetically levitated above a spherical magnet, as schematically shown in Fig. 3. We model this setup as the levitation of a superconducting ring of finite thickness above a spherical small magnet. The magnetic field of a uniformly magnetized sphere is exactly that from a magnetic dipole [52], and the case of an infinitesimally thin superconducting ring levitated above a point magnetic dipole can be analyzed analytically [53]. We assume the origin of the coordinate system is at the center of the ring. The ring is cooled to a superconducting state subject to the zero-field condition, and then moved above the magnet with magnetization $m_{\mathrm{mag}}\vec{z}$. To maintain the flux threading conservation, a current is induced in the ring with $I = \mu_0 m_{\mathrm{mag}} R^2/(2L(z^2+R^2)^{3/2})$, where $R$ is the radius of the ring, $|z|$ is the distance from the magnet to the center of the ring, and $L = \mu_0 R \ln[8R/r] - 2$ is the self-inductance of the ring [53]. The current-carrying ring in the field of the magnet feels a repulsive force that is equal and opposite to the force on the magnet in the field generated by the ring $F_{\mathrm{ring}} = (\partial B_z/\partial z) m_{\mathrm{mag}}$. The equilibrium separation between the magnet and the ring $|z| = h$ can be solved by one equating the magnetic force $F_{\mathrm{ring}}$ to the force of gravity acting on the ring $Mg$:

$$\frac{3\mu_0^2 m_{\mathrm{mag}}^2 R^4 z}{4L(z^2+R^2)^4} = Mg. \tag{7}$$

The vertical trap frequency is obtained from $\omega_z = 2\pi v_z = \sqrt{k/M}$, where $k = -\partial F_{\mathrm{ring}}/\partial z|_{|z|=h}$ is the spring constant, as

$$v_z = \frac{1}{2\pi}\sqrt{\frac{3\mu_0^2 m_{\mathrm{mag}}^2 R^4(-7h^2+R^2)}{4L(h^2+R^2)^5 M}}. \tag{8}$$

In addition to the persistent current–generated repulsive force between the ring and the magnet, there is also an additional force due to the superdiamagnetism (Meissner) of the superconducting ring interacting with the magnet, but the latter is much smaller. This superdiamagnetism force plays a crucial role in providing the horizontal and tilt stability of the levitated ring (see Appendix C for more details).

To generate a superposition state, we consider an additional superconducting driver circuit situated nearby the flux qubit without any direct mechanical contact to inductively drive the flux qubit. The supercurrent in this driver circuit can generate a magnetic field to change the magnetic flux threading the flux qubit and thereby can inductively drive the flux qubit into the current superposition of $|0\rangle$ or $|1\rangle$ states. The flux qubit when in the state $|q\rangle$, $q = 0, 1$, generates a state-dependent magnetic field and field gradient

$$B_z(z)_{|q\rangle} = (-1)^q \frac{\mu_0 |I| R^2}{2(z^2+R^2)^{3/2}}, \tag{9}$$

$$\left(\frac{\partial B_z}{\partial z}\right)_{|q\rangle} = (-1)^{q+1} \frac{3\mu_0 |I| R^2 z}{2(z^2+R^2)^{5/2}}. \tag{10}$$

The force on the flux qubit is again equal and opposite to that on the magnet, and can be computed as

$$F_{\mathrm{FQ}}^{|q\rangle} = -\vec{m}_{\mathrm{mag}} \cdot (\partial \vec{B}_z/\partial z)_{|q\rangle}. \tag{11}$$

At the equilibrium height $|z| = h$, the force on the qubit in state $|q\rangle$ is given by

$$F_{\mathrm{FQ}}^{|q\rangle} = (-1)^q \frac{3\mu_0 |I| R^2 h m_{\mathrm{mag}}}{2(h^2+R^2)^{5/2}}. \tag{12}$$

Because of this $F_{\mathrm{FQ}}^{|q\rangle}$, the equilibrium height of the flux qubit shifts to a position, $z_\pm = \pm z_{\mathrm{eq}}$, depending on the state of the flux qubit (we choose the $z$ origin to be at the equilibrium height when there is no inductive driving). At these offset equilibria the offset force $\vec{F}_{\mathrm{FQ}}$ is balanced by the trapping force $|F_{\mathrm{tr}}| = 2\pi^2 r^2 \rho R \omega_z^2 z_{\mathrm{eq}}$, giving $\vec{F}_{\mathrm{FQ}}^{|q\rangle} + \vec{F}_{\mathrm{tr}} = 0$. We analytically estimate the spatial separation $\Delta z$ between these two equilibrium heights as

$$\Delta z = 2z_{\mathrm{eq}} \sim \frac{3\mu_0 m_{\mathrm{mag}} |I| R h}{2\pi^2 r^2 (h^2+R^2)^{5/2} \rho \omega_z^2} \tag{13}$$

when $\Delta z \ll h$.

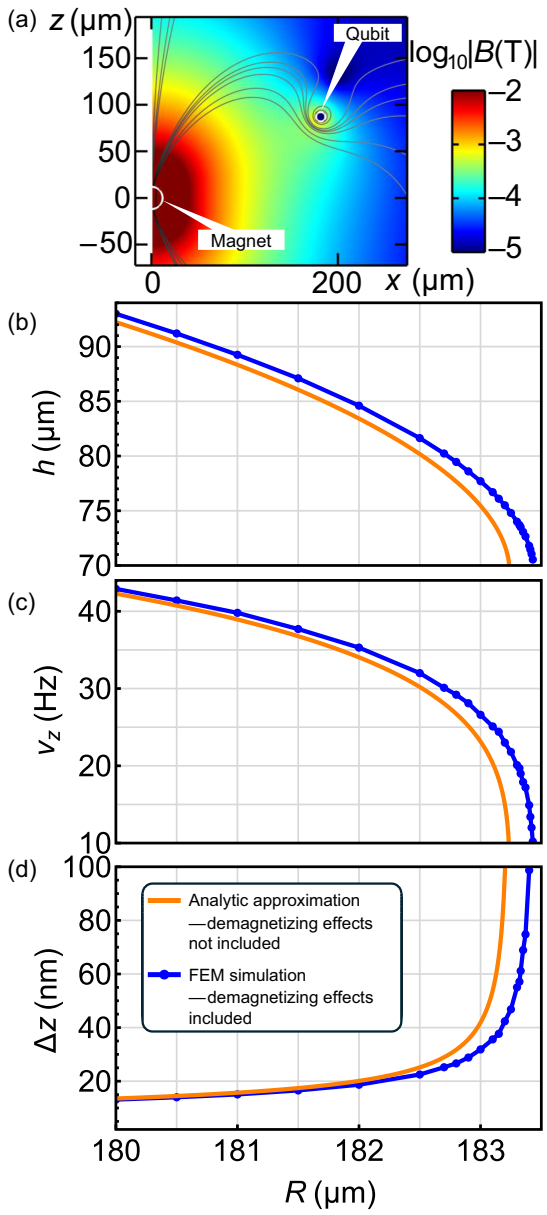



FIG. 4. Numerical FEM simulation results for the trapped superconducting flux qubit and its motional superposition. (a) Magnetic flux density $B$ in the axisymmetric cross section for a magnetic trap where a flux qubit of radius $R = 183.4$ μm is levitated $h = 71.8$ μm above a spherical magnet with radius $r = 12$ μm. We can see the effect of the demagnetizing field of the superconductor on the magnetic field around the levitated flux qubit. (b) Equilibrium position, (c) trap frequency, and (d) superposition separation extent in the $z$ direction as a function of $R$. For qualitative comparison, analytical approximations [Eq. (7) for $h$ in (b), Eq. (8) for $\nu_z$ in (c), and Eq. (13) for $\Delta z$ in (d)] that do not include the demagnetizing effects are plotted as orange curves.

The above estimate assumed the flux qubit is modeled as an infinitesimally thin superconducting ring. To account for a more realistic case where the superconducting ring has finite thickness, we must consider the effects of the demagnetizing field generated by the superconductor on the magnetic fields levitating the ring. These demagnetizing fields essentially cause all energetic fields within the superconductor to vanish. To take this effect into account, we use a finite element method (FEM) COMSOL MULTIPHYSICS simulation (blue curves in Fig. 4). The analytical model in Ref. [53] does not include this demagnetizing effect, the predictions of [53] are shown for comparison (orange curves in Fig. 4). We are unaware of any published analytical study that includes the demagnetizing field, so in Appendix D we derive an instructive analytical solution for a simpler example including such demagnetizing effects. We present the numerical results in Fig. 4 (blue curves), which are comparable with the analytical approximations (orange curves). In Fig. 4(a), we observe a significant perturbation of the fields surrounding the flux qubit, which is expected due to the demagnetizing field of the superconducting ring, and can see that the magnetic field strength $|B|$ at the location of the ring is less than 1 mT. From Fig. 4(a), we can see that as $R$ increases, the magnetic field seen by the flux qubit decreases, and we expect the trapping stiffness (and thereby $\omega_z$ and $h$) to drop as $R$ increases. We observe this in Figs. 4(b) and 4(c), with a critical value of the radius above which the flux qubit cannot be stably trapped. We show $\Delta z$ in this region in Fig. 4(d), and find that $\chi \sim 10^6$ when $R \sim 183.4$ μm (corresponding to $\Delta z \sim 100$ nm and $\nu_z \sim 15$ Hz). Larger values of $\Delta z$ are predicted from theory but are probably not feasible in experiments.

## III. DECOHERENCE

Decoherence is a limiting factor for the generation of a large superposition state in our systems. Thus, the coherence time of the mechanical oscillator and that of the flux qubits are important in our schemes.

The decoherence of mechanical oscillation of the levitated objects arises from the undesired interactions of the oscillators with the surroundings [54]. To minimize the interaction of the levitated particle with the surroundings that causes mechanical damping, we consider the following situations. In the first scheme, we consider YIG, which is a soft magnet. The eddy damping within YIG itself is negligible because it is an electrical insulator [55]. However, the motion of the oscillator (YIG) may cause eddy damping within the conductors surrounding the oscillator. We can consider the use of superconducting shields to isolate the trap from other conductors, and it can also screen the external electric and magnetic noise as well. In the second scheme, the magnet used to lift the ring can be machined with insulating ferrite to avoid eddy damping. To minimize decoherence due to nearby charge fluctuations, we consider that the levitated objects are electrically neutral. This can be achieved with ultraviolet illumination to remove all stray charges on the levitated objects [56]. By theoretically probing the various sources of decoherence

in more detail, we identify that gas molecule collision is the dominant damping and decoherence source for our mechanical oscillators (see Appendix E for more details). We assume that the levitated system is sufficiently isolated in the dilution fridge to keep the vibration noise level on the oscillators at $10^{-16}\, g/\sqrt{\text{Hz}}$ or less, where $g$ is the gravitational acceleration. For this, a dilution fridge with pulse tube shutoff should be used to avoid pulse tube noise [57,58] and/or multiple stages of active and passive vibration isolation systems should be used to suppress the ground vibration noise [59–62]. Thus, the dominant decoherence rate, which is due to the damping induced by the surrounding gas collisions, is then

$$\Gamma_{\text{g}} = \frac{\gamma_{\text{g}}}{\lambda_{\text{dB}}^2}(\Delta z)^2, \tag{14}$$

where $\gamma_{\text{g}}$ is the energy damping rate of the oscillator due to the gas collisions and $\lambda_{\text{dB}} = \hbar(\sqrt{2\pi/Mk_{\text{B}}T})$ is the de Broglie wavelength of the oscillator, with $k_{\text{B}}$ the Boltzmann constant. We define the motional damping rate as $\gamma_{\text{g}}$, where $\gamma_{\text{g}} = \omega_z/Q$, where $Q$ is the quality factor of the oscillator. For the two types of oscillator we are considering, $Q$ can be generally written as [49,63] (see Appendix E for more details)

$$Q \approx \frac{\pi\rho r\omega_z}{6P_{\text{g}}}\sqrt{\frac{3k_{\text{B}}T}{M_{\text{g}}}}, \tag{15}$$

where $M_{\text{g}}$ is the mass of the gas molecule and $r$ is the cross-section radius of a spherical (toroidal) oscillator. To minimize gas collisions one must operate in the regime of an extremely high vacuum, with pressures $P_{\text{g}} = 10^{-16}$ mbar, which is experimentally feasible with use of the cyropumping effect [64]. To achieve this the vacuum chamber must be operated at low temperatures $T$ on the order of millikelvins, but such low temperatures are required in any case for the flux qubit operation. For a YIG sphere with a radius of 25 μm, we estimate $Q \sim 3.3 \times 10^{15}$ due to the gas collisions. Similarly, for the flux qubit ring we estimate the gas collision–limited $Q \sim 3.5 \times 10^{14}$. The $Q$ factor, or quality factor, describes the rate of energy loss by the damped oscillator. The rate of loss of the quantum coherence of a large superposition is known as the decoherence rate, and this is usually higher than the rate of loss of energy. This decoherence rate scales quadratically with the size of the superposition $\Delta z$. Assuming $\Delta z = 1$ nm, we can estimate the decoherence rate due to gas collisions $\Gamma_{\text{g}}$ for the YIG sphere (flux qubit ring) to be 12 Hz (87 Hz), corresponding to a coherence time $1/\Gamma_{\text{g}} = 79$ ms (11 ms; see Appendix E.

We consider type I superconductors (aluminum for flux qubits, and lead for the magnetic trap and shields) for our schemes to avoid flux creep, which is an issue in type II superconductors and should not be present in type I high-purity superconductors. We assume that the operating temperatures for our schemes are around 10 mK (which can be achieved with a dilution fridge) to ensure that we are in a deeply superconducting regime and to suppress decoherence effects on the flux qubits. In our schemes, the magnetic field strengths at the location of the flux qubits are well below the critical magnetic field strength of 9.78 mT [65]. Aluminum superconducting wire at low temperatures has a critical current density $I_{\text{c}} \sim 10^{10}$ A/m$^2$ [66]. For our rings with a cross-section radius of 5 μm, we verify that the critical current (approximately 1 A) is much higher than any supercurrent considered in the present study, ensuring the superconducting state for the flux qubits.

To achieve $\chi \sim 10^6$ ($\Delta z \sim 100$ nm) with our schemes, an evolution time of half a trap period is required, which is approximately 50 ms (corresponding to very low trap frequencies of approximately 10 Hz). To achieve $\chi \sim 10^4$ ($\Delta z \sim 1$ nm), we can increase the trap frequency, and the coherence time required can be reduced to approximately 100 μs. The state-of-the-art flux qubits have coherence times approaching 100 μs, which can be further increased [67,68]. As we discussed above, mechanical oscillators with ultrahigh motional $Q$ are extremely isolated and can preserve the motional coherence for tens of milliseconds. Thus, an ultralarge spatial superposition with $\chi \sim 10^4$ can be experimentally realized with flux qubits that already exist today.

The state purity (e.g., spatial quantum coherence length) provides another quantification of the degree of nonclassicality of the decohering quantum superposition. Our estimates of decoherence rates suggest that spatial quantum coherence can be maintained over timescales relevant for the generation of the superposition. In the large-$t$ limit (for times longer than the localization timescale), the coherence length can be approximated as $\ell(t) \sim 1/\sqrt{2(\gamma_{\text{g}}/\lambda_{\text{dB}}^2)t}$ [69]. Assuming $\Delta z = 1$ nm and decoherence rate $\Gamma \sim 12$ Hz, one finds $\ell(1\text{ ms}) \sim 9$ nm, which is greater than $\Delta z$, indicating that by 1 ms the spatial quantum coherence of the superposition is still very good (see Appendix E).

Realizing a much larger superposition, with $\chi \sim 10^6$, will require a much lower decoherence rate. The experiment should be implemented at low pressure to reduce the decoherence of the mechanical motion caused by gas collisions. Our proposals apply to any flux-based superconducting qubit whose qubit states are defined by large circulating persistent currents. The fluxonium qubit, which has reached millisecond coherence times [70,71], is a potential candidate.

## IV. PREPARATION AND WITNESSING OF THE SUPERPOSITION

To prepare and witness the superpositions we adapt a Ramsey interferometry protocol similar to that in Ref.

[72,73]. We can apply this Ramsey sequence to both schemes—levitated magnet and flux qubit—to witness the superposition. We assume the resonator is initially in the $|0\rangle$ state and the resonator is in a motional coherent state $|\psi\rangle \sim |\alpha\rangle \bigotimes |0\rangle$, and the Ramsey sequence consists of four steps: (1) apply a $\pi/2$ pulse at time $t_0 = 0$ to generate a superposition state; (2) apply a $\pi$ pulse at time $t_1 = \tau$ to flip the qubit state; (3) apply another $\pi$ pulse at time $t_2 = t_1 + \tau'$ to flip the qubit state again; (4) apply another $\pi/2$ pulse at time $t_3 = t_2 + \tau$ and get the final state $|\psi\rangle \sim |\alpha\rangle \bigotimes (\cos(\phi_{\rm grav}/2)|0\rangle + \sin(\phi_{\rm grav}/2)|1\rangle)$ to reveal $\phi_{\rm grav}$. The population of state $|0\rangle$ is given by $P_0 = \cos^2(\phi_{\rm grav}/2)$. The gravity-induced phase difference $\phi_{\rm grav} = Gg\cos\theta\sqrt{2M/\hbar\omega_z^3}\Delta t$, where $g$ is the gravitational acceleration, $\theta$ is the angle between the vertical axis and the $z$ axis, $M$ and $\omega_z$ are the mass and mechanical frequency of the resonator, $\Delta t = 2\tau - \tau'$, and $G = m(\partial B/\partial z)\delta z_{\rm ZPM}/2\pi\hbar$ is the coupling strength, where $m$ is the magnetic moment of the magnet, $\partial B/\partial z$ is the gradient of the magnetic field generated by the flux qubit (qubits), and $\delta z_{\rm ZPM} = \sqrt{\hbar}/2M\omega_z$ is the zero-point motional extent of the resonator, respectively. We can expand the coupling strength as $G = AB_r r^3 I\delta z_{\rm ZPM}/2\pi R^2\hbar$, where $A$ is a dimensionless coefficient, $B_{\rm r}$ and $r$ are the remanent magnetization and radius of the magnet, respectively, and $I$ and $R$ are the current and radius of the flux qubit, respectively. In the first scheme, $A = 4\pi(\eta/(1+\eta^2)^{5/2}) \approx 3.6$, and in the second scheme, $A = 2\pi(\eta/(1+\eta^2)^{5/2}) \approx 1.7$. Here $\eta$ is the ratio of the distance between the spherical magnet and the center of the flux qubit to the radius $R$ of the flux qubit in both schemes. We obtain coupling strengths $G/2\pi \approx 1.3\times10^6$ Hz ($9.4\times10^6$ Hz) in the first (second) scheme

## V. CONCLUSION

In summary, we present two complementary schemes to generate massive spatial superpositions on a levitated system based on the superposition of magnetic forces generated by flux qubits. We show that the ratio of the spatial superposition separation to the motional ground state width $\chi$ can be on the order of $10^4$–$10^6$. The analyses based on experimental considerations suggest that the experimental realization of our schemes is within reach and thus could pave the way to ultrasensitive quantum sensing applications.

## ACKNOWLEDGMENTS

This research was supported by the Australian Research Council Centre of Excellence for Engineered Quantum Systems (Grant No. CE170100009) and the Okinawa Institute for Science and Technology Graduate University. S.B. acknowledges EPSRC Grant No. EP/X009467/1 and STFC Grant No. ST/W006227/1.

## DATA AVAILABILITY

The data are not publicly available. The data are available from the authors upon reasonable request.

## APPENDIX A: MAGNETIC TRAP FOR THE YIG SPHERE

The YIG sphere can be levitated above a superconducting block with a rectangular hole (as shown in Fig. 5). The size and depth of the hole determine the horizontal trap frequencies. The equilibrium height of a magnet above an infinite superconducting plate was analytically worked out in Ref. [74]. We simulated, using the finite element program COMSOL MULTIPHYSICS, the levitation of the YIG sphere above a finite superconducting block with a rectangular indentation as a spatial trap for the YIG. As expected, the COMSOL MULTIPHYSICS simulation results converge to the analytical predictions based on Ref. [74] as the dimensions of the superconductor block becomes larger (see Fig. 6). The simulation also shows that the magnetic sphere ($R = 25$ μm) can be stably levitated above a small superconducting block (e.g., $a = b = 70$ μm) whose size fits between the two flux-based qubits. The COMSOL MULTIPHYSICS simulation shows that we can engineer the horizontal motional frequency to be extremely low. This levitation setup is small and compact.

## APPENDIX B: EFFECT OF MAGNETIC FIELD GENERATED BY YIG ON THE FLUX QUBIT

We assumed that the magnetic field produced by the spherical magnet at the location of the superconducting

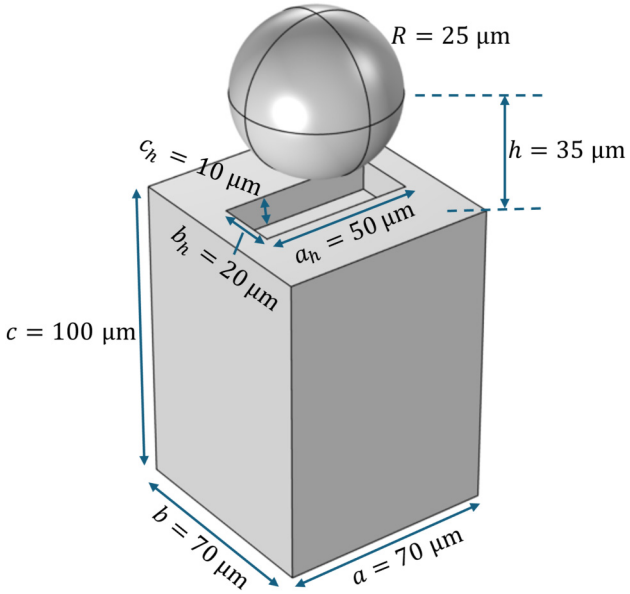



FIG. 5. Levitated YIG magnet sphere and the superconducting trap with a shallow rectangular hole. The YIG magnet sphere with magnetization $B_r = 14.32$ mT and radius $R = 25$ μm is levitated at $h = 35$ μm (the center of the sphere is above the top surface of the superconductor block).

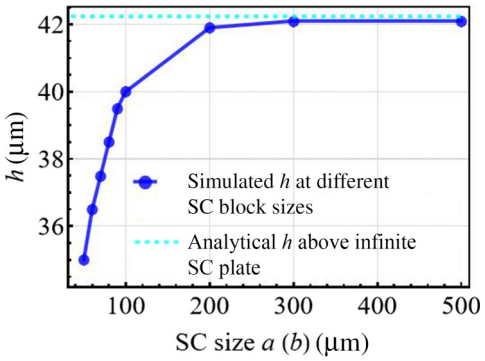



FIG. 6. Equilibrium height $h$ of the YIG magnet sphere ($R = 25$ μm) above the SC block with different sizes. The dashed cyan line shows $h$ of the magnet above an infinite SC plate, adapted from Ref. [74]. The solid blue line represents the simulated $h$ of the sphere above a SC block with fixed thickness ($c = 100$ μm) but different widths (lengths) ($a = b$) in the range of 50–500 μm.

material is below the critical magnetic field of 9.8 mT for aluminum. To verify this assumption, we consider a spherical magnet of radius 25 μm (other parameters are given in Table I) using RADIA in MATHEMATICA. RADIA is a three-dimensional (3D) magnetostatics computer code optimized for solving boundary magnetostatics problems with magnetized and current-carrying volumes using the boundary integral approach [75]. We modelled the spherical magnet using "radObjMltExtPgn" function in RADIA with magnetization along $x$ and $y$ axis set to zero, and along $z$-axis set to $B_r$ value in Table I. We simulated the magnetic field (along $z$-axis, i.e, $B_z$) as a function of $x$ values for different $z$ values, and the results are shown in Fig. 7. Verifying all the values presented in Fig. 7 analytically is not possible. However, we verified that the magnetic field values for different $z$ values presented here for $x = 0$, is matching with analytical expression of the magnetic field generated by a dipole given as $(\mu_0|m_0|)/(2\pi z^3)$ by assuming the spherical magnet as a point dipole. From the results presented in Fig. 7, we can see that the assumption is valid for the YIG sphere size presented here.

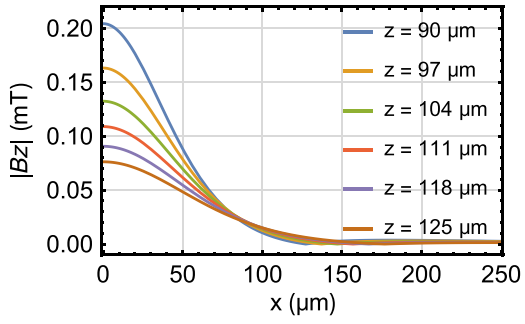



FIG. 7. Absolute value of the magnetic field $z$ component generated by the magnetic sphere as a function of the $x$ position for two different $z$ positions as denoted by the legends. The solid curves correspond to the magnetic sphere at the origin and the dashed curves correspond to when the magnetic sphere is shifted to $z = 1$ μm.

## APPENDIX C: HORIZONTAL STABILITY OF THE LEVITATED FLUX QUBIT

We now study the lateral trapping of the levitated flux qubit and will see that it is stably trapped for both small shifts in the lateral position and for small tilts. We model the levitated flux qubit as a superconducting ring with finite thickness and include the superdiamagnetism and demagnetizing fields, using COMSOL MULTIPHYSICS. We find both motions are trapped and stable, confirming the complete trapping of the six degrees of freedom of the levitated flux qubit. We simulate the levitation of superconducting flux qubit using the spherical micromagnet in a 2D axisymmetric model using the FEM package COMSOL MULTIPHYSICS. In this FEM model, we consider the flux qubit as a superconducting ring with the ideal Meissner effect. We find that the London penetration has a negligible effect on the results due to the large size of the flux qubit. Furthermore, by performing a fully 3D FEM COMSOL MULTIPHYSICS simulation, we determined that the levitated flux qubit is stable both vertically and horizontally, due to the loop shape of

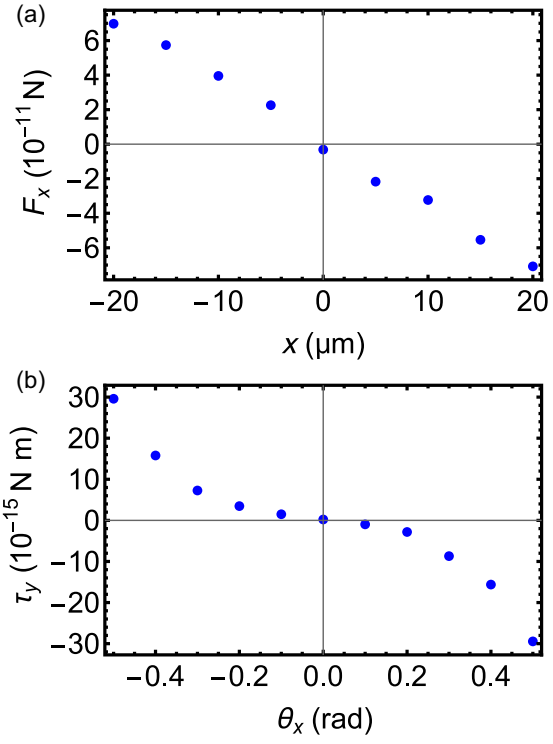



FIG. 8. Horizontal stability of the levitated superconducting flux qubit. (a) Magnetic force $x$ component $F_x$ as a function of the $x$-direction horizontal displacement of the trapped flux qubit. (b) Torque $y$ component $\tau_y$ as a function of the tilting angle around $y$. The data were numerically calculated in a full 3D COMSOL MULTIPHYSICS model with flux qubit radius $R = 183$ μm.

the flux qubit. We observe that the magnetic forces and torques will work to restore the qubit's equilibrium position and orientation when the flux qubit horizontally shifts or tilts slightly. Thus, the trapped flux qubit experiences complete rigid-body trapping. It is worth noting that Navau *et al.* [53] expressed concern about the lack of horizontal stability in the case of an infinitely thin ring. However, for a real superconducting ring with finite thickness, the Meissner effect of the bulk superconductor will act to keep the ring horizontally stable.

To test the horizontal stability of the trapped flux qubit, we built a full 3D COMSOL MULTIPHYSICS model. In this model, we calculated the $x$-component magnetic force $F_x$ under the condition of horizontal displacement $x$ (see Fig. 8). We found that the magnetic force acts as a restoring force when the flux qubit shifts away from the central position in the horizontal direction. Also, when the qubit is tilted, a magnetic torque builds up on the flux qubit to restore it to its original horizontal orientation. We predict that the levitated flux qubit will be unstable when the horizontal displacement (or tilting) is too large. We have also calculated the horizontal trap frequency as approximately 19 Hz and the tilting frequency as approximately 9 Hz.

## APPENDIX D: DEMAGNETIZATION EFFECT OF SUPERCONDUCTORS

To illustrate the effect of the demagnetizing field and how this can be studied analytically, we consider a simpler example setup: the diamagnetic trapping of a SC sphere by two nearby homogeneous magnetic spheres (which we consider as magnetic dipoles) arranged in an anti-Helmholtz configuration. We derive an analytical solution for the trap properties along the trapping axis using an exact method not described before in the literature to the best of our knowledge. We find that the key parameter, the vertical trap stiffness, is modified by almost 62.5% from the case when no demagnetizing field is considered, and the FEM package COMSOL MULTIPHYSICS provides results that match very well with the analytical solution of this example.

We show the demagnetizing field of the superconductor on the magnetic field used to trap it by considering the example of trapping a SC sphere using two dipoles in an anti-Helmholtz magnetic configuration (magnetic moments antiparallel). This anti-Helmholtz magnetic configuration can be realized experimentally either with current-carrying loops as in Sec. II A, where the first method was introduced, or with uniformly magnetized spherical magnets to produce an external magnetic field that is identical to a point magnetic dipole [76].

We first note that a number of authors have considered analytical treatments of the Meissner force of a SC sphere in anti-Helmholtz magnetic fields [77,78] as well as the force between a point dipole and a SC sphere [79,80].

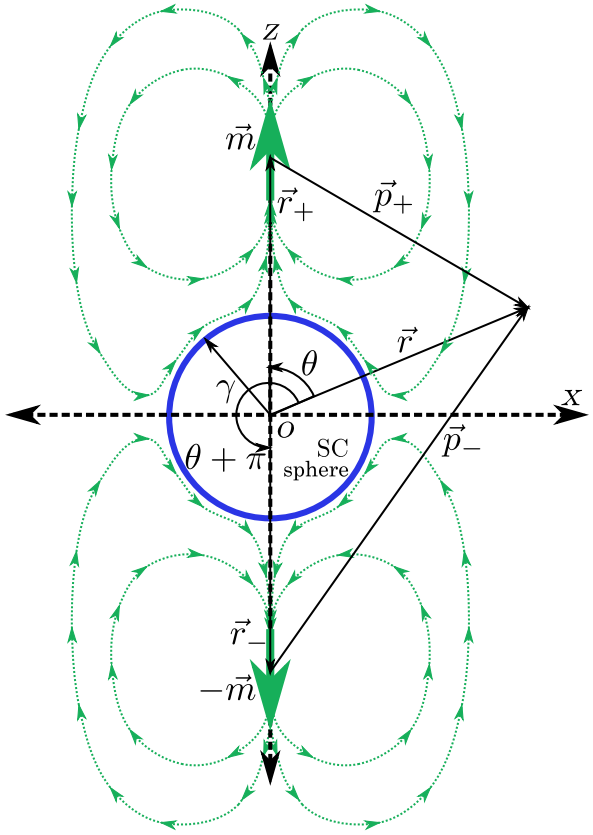



FIG. 9. Schematic diagram for the analytical derivation of the magnetic trap properties in the $z$ direction. The SC sphere with radius $\gamma$ located at the origin $O$ is shown as a blue circle. Magnetic dipoles with moment $\vec{m}$ and $-\vec{m}$ are shown as thick green arrows and their field lines are represented by dotted green arrows. $\vec{r}_+$ and $\vec{r}_-$ are the vectors from the origin to magnetic dipoles $\vec{m}$ and $-\vec{m}$, respectively. An arbitrary point is chosen for the generalized derivation, and $\vec{r}$ is shown from the origin to this arbitrary point. $\vec{p}_+$ and $\vec{p}_-$ are, respectively, the vectors from magnetic dipoles $\vec{m}$ and $-\vec{m}$ to the arbitrary point of interest.

Many of these studies used the image method, but there seems to be some concern in the literature regarding this method [81], and so we do not use the image method in what follows, and we solve for the magnetic fields and associated forces directly.

We consider the magnets and the SC sphere to have centers that all lie on the $z$ axis, and we visualize the geometry in the $x$-$z$ plane as shown in Fig. 9. We analytically derive the induced magnetic field at the SC sphere due to the magnetic field of the two point dipoles, using scalar potentials of the dipoles and enforcing the appropriate boundary conditions at the surface of the SC sphere. Then we derive an expression for the levitation force by considering the interaction between the resulting magnetic field and the two point dipoles.

We denote $\Phi_+$ and $\Phi_-$ to be the scalar potentials of the two dipoles located, respectively, at $\vec{r}_+ \sim (0, 0, d_+)$

and $\vec{r}_- \sim (0,0,-d_-)$ at either side of the origin along the $z$ axis. At the arbitrary point $\vec{r} \sim (x,y,z)$, these scalar potentials can be written as [79,82]

$$\Phi_\pm(\vec{r}) = \pm\frac{\mu_0}{4\pi}\frac{\vec{m}\cdot\vec{p}_\pm}{||\vec{p}_\pm||^3}, \tag{D1}$$

where $\mu_0$ is the magnetic permeability of free space and $\vec{p}_\pm = \vec{r} - \vec{r}_\pm$. In spherical coordinates with radius $\vec{r}$, polar angle $\theta$, and azimuthal angle $\phi$, Eq. (D1) can be rewritten as

$$\Phi_\pm(\tilde{r}_\pm,\theta) = \frac{\mu_0 m}{4\pi d_\pm^2}\frac{((\pm\tilde{r}_\pm)\cos\theta - 1)}{\left((\pm\tilde{r}_\pm)^2 - 2(\pm\tilde{r}_\pm)\cos\theta + 1\right)^{\frac{3}{2}}}, \tag{D2}$$

where $m = ||\vec{m}||$ and $\tilde{r}_\pm = r/d_\pm$. There is no $\phi$ dependency due to the axial symmetry of the system. By expansion using Legendre polynomials, Eq. (D2) can be written as

$$\Phi_\pm(\tilde{r}_\pm,\theta) = -\frac{\mu_0 m}{4\pi d_\pm^2}\sum_{n=0}^{\infty}(n+1)\,(\pm\tilde{r}_\pm)^n\,P_n(\cos\theta). \tag{D3}$$

Then the net scalar potential ($\Phi_\mathrm{m} \equiv \Phi_+ + \Phi_-$) generated by the two dipoles can be written as

$$\Phi_\mathrm{m}(\mathrm{r},\theta) = -\frac{\mu_0 m}{4\pi}\sum_{n=0}^{\infty}(n+1)r^n P_n(\cos\theta) \times\left[\left(\frac{1}{d_+}\right)^{n+2} + \left(-\frac{1}{d_-}\right)^{n+2}\right]. \tag{D4}$$

The radial component of the magnetic field generated by the two dipoles is given by $\vec{B}_\mathrm{r,m} = -\hat{r}\frac{\partial\Phi_\mathrm{m}}{\partial r}$, and in our case we find

$$\vec{B}_{r,\mathrm{m}}(\mathrm{r},\theta) = \hat{r}\frac{\mu_0 m}{4\pi}\sum_{n=0}^{\infty}n(n+1)r^{(n-1)}P_n(\cos\theta) \times\left[\left(\frac{1}{d_+}\right)^{n+2} + \left(-\frac{1}{d_-}\right)^{n+2}\right]. \tag{D5}$$

We use the subscript $r$ to indicate that we compute only the radial component of $\vec{B}$, and the subscript $m$ indicates that the magnetic field is due to the dipoles and without the SC sphere. Introduction of the SC sphere results in the introduction of an additional effective magnetic field in response to the field due to the dipoles. Taken together, the induced and dipole fields must satisfy the Meissner boundary conditions, that the total magnetic field has a vanishing orthogonal component at all superconducting surfaces.

We write down a general solution for the scalar potential corresponding to an induced magnetic field of the SC sphere, due to the Meissner effect, as

$$\Phi_\mathrm{SC}(\mathrm{r},\theta) = \sum_{n=0}^{\infty}\frac{C_n}{r^{(n+1)}}P_n(\cos\theta)\,,\ r > \gamma, \tag{D6}$$

where $C_n$ is a general coefficient that has to be determined and $\gamma$ is the radius of the SC sphere. This gives a magnetic field in the radial direction as

$$\vec{B}_\mathrm{r,SC}(r,\theta) = \hat{r}\sum_{n=0}^{\infty}(n+1)\frac{C_n}{r^{(n+2)}}P_n(\cos\theta)\,. \tag{D7}$$

We now express the total radial component of the magnetic field as $\vec{B}_\mathrm{r,T} = \vec{B}_\mathrm{r,m} + \vec{B}_\mathrm{r,SC}$. Considering the perfect Meissner state for the SC sphere, we must have $\vec{B}_\mathrm{r,T}(r=\gamma,\theta) = 0$ for all $\theta$. This permits us to fix $C_n$ as

$$C_n = -\frac{\mu_0 m}{4\pi}n\gamma^{(2n+1)}\left[\left(\frac{1}{d_+}\right)^{n+2} + \left(-\frac{1}{d_-}\right)^{n+2}\right]. \tag{D8}$$

Inserting Eq. (D8) into Eqs. (D6) and (D7), we obtain the scalar potential and the radial component of the induced magnetic field of the SC sphere as

$$\Phi_\mathrm{SC}(\mathrm{r},\theta) = -\frac{\mu_0 m}{4\pi}\sum_{n=0}^{\infty}n\frac{\gamma^{(2n+1)}}{r^{(n+1)}}P_n(\cos\theta) \times\left[\left(\frac{1}{d_+}\right)^{n+2} + \left(-\frac{1}{d_-}\right)^{n+2}\right], \tag{D9}$$

$$\vec{B}_{r,\mathrm{SC}}(r,\theta) = -\hat{r}\frac{\mu_0 m}{4\pi}\sum_{n=0}^{\infty}n(n+1)\frac{\gamma^{(2n+1)}}{r^{(n+2)}}P_n(\cos\theta) \times\left[\left(\frac{1}{d_+}\right)^{n+2} + \left(-\frac{1}{d_-}\right)^{n+2}\right]. \tag{D10}$$

Choosing $\theta = 0$ and $\theta = \pi$, we can obtain the magnetic field at the location of the SC sphere along the $z$ axis from the radial component of the magnetic field. For comparison with the numerical simulations reported below, we now convert the magnetic field back to Cartesian coordinates and obtain

$$\vec{B}^\pm_\mathrm{m}(z) = \pm\hat{k}\frac{\mu_0 m}{4\pi}\sum_{n=0}^{\infty}n(n+1)\,(\pm z)^{(n-1)}\,P_n(\pm1) \times\left[\left(\frac{1}{d_+}\right)^{n+2} + \left(-\frac{1}{d_-}\right)^{n+2}\right], \tag{D11}$$

where now $+$ and $-$ in $\pm$ correspond to, respectively, positive and negative values for the $z$ axis and $\hat{k}$ is the unit

vector along the $z$ axis. Similarly, we find for the magnetic field induced by the SC sphere with radius $\gamma$

$$\vec{B}^{\pm}_{\mathrm{SC}}(z) = \mp\hat{k}\frac{\mu_0 m}{4\pi}\sum_{n=0}^{\infty} n(n+1)\frac{\gamma^{(2n+1)}}{(\pm z)^{(n+2)}}P_n(\pm 1) \times\left[\left(\frac{1}{d_+}\right)^{n+2}+\left(-\frac{1}{d_-}\right)^{n+2}\right]. \tag{D12}$$

From Eqs. (D11) and (D12) we obtain

$$\vec{B}_{\mathrm{m}}(z) = \vec{B}^{\pm}_{\mathrm{m}}(z) = -\hat{k}\frac{\mu_0 m}{2\pi}\left[\frac{1}{(z-d_+)^3}+\frac{1}{(z+d_-)^3}\right], \tag{D13}$$

$$\vec{B}^{+}_{\mathrm{SC}}(z) = -\vec{B}^{-}_{\mathrm{SC}}(z) = \hat{k}\frac{\mu_0 m}{2\pi}\gamma^3 \times\left[\frac{1}{\left(\gamma^2-zd_+\right)^3}+\frac{1}{\left(\gamma^2+zd_-\right)^3}\right]. \tag{D14}$$

Then the net magnetic field along the $z$ axis between the two dipoles with the SC sphere is given by the piecewise function

$$\vec{B}_{\mathrm{T}}(z) = \begin{cases}\vec{B}_{\mathrm{m}}(z)+\vec{B}^{+}_{\mathrm{SC}}(z), & z>\gamma,\\ 0, & -\gamma\le z\le\gamma,\\ \vec{B}_{\mathrm{m}}(z)+\vec{B}^{-}_{\mathrm{SC}}(z), & z<-\gamma.\end{cases} \tag{D15}$$

Without the SC sphere present between the two dipoles, $\vec{B}_{\mathrm{T}}(z) = \vec{B}_{\mathrm{m}}(z)$.

We compute the $z$ component of the force on the SC sphere and from the dipoles as

$$\vec{F}_{\mathrm{SC}}(d_+,d_-) = -\hat{k}\frac{\partial}{\partial z}\left(\vec{m}\cdot\vec{B}^{+}_{\mathrm{SC}}(z)\right)\Big|_{z=d_+} + \hat{k}\frac{\partial}{\partial z}\left(\vec{m}\cdot\vec{B}^{-}_{\mathrm{SC}}(z)\right)\Big|_{z=d_-}. \tag{D16}$$

The final form of $\vec{F}_{\mathrm{SC}}$ is given by

$$\vec{F}_{\mathrm{SC}} = \hat{k}\frac{3}{2}\frac{\mu_0 m^2}{2\pi}\gamma^3\left[\frac{2d_-}{\left(\gamma^2-d_-^2\right)^4}-\frac{2d_+}{\left(\gamma^2-d_+^2\right)^4} + \frac{d_-}{\left(\gamma^2+d_+d_-\right)^4}-\frac{d_+}{\left(\gamma^2+d_+d_-\right)^4}\right]. \tag{D17}$$

The properties of the trap can be explored by our introducing displacements to the SC sphere. For this, we consider two parameters: the total gap between the centers of two magnets $d = d_+ + d_-$ and the displacement $2\delta = d_- - d_+$. Then with the transformation $d_{\mp} = (d/2)\pm\delta$, we can write $\vec{F}_{\mathrm{SC}}$ as a function of $\delta$. We perform a series expansion of such a function, and from this series, which consists only of odd terms, we approximately ignore all the higher-order terms assuming small displacements but the first-order term. The resultant $\vec{F}_{\mathrm{SC}}(\delta)$ can be written as

$$\vec{F}_{\mathrm{SC}}(\delta) \sim -\hat{k}384\frac{\mu_0 m^2}{\pi}\gamma^3\left[\frac{14d^2+8\gamma^2}{(d^2-4\gamma^2)^5}-\frac{1}{(d^2+4\gamma^2)^4}\right]\delta. \tag{D18}$$

When the separation between dipoles is much greater than the diameter of the SC sphere, $d \gg 2\gamma$, $\vec{F}_{\mathrm{SC}}(\delta)$ can be written as

$$\vec{F}_{\mathrm{SC}}(\delta) \sim -\hat{k}4992\frac{\mu_0 m^2}{\pi}\frac{\gamma^3}{d^8}\delta. \tag{D19}$$

The magnitude of force in Eq. (D19) is of the form of $F_{\mathrm{SC}}(\delta) = -k_z\delta$, where $k_z = 4992\mu_0 m^2\gamma^3/\pi d^8$ is the spring constant or stiffness of the trap. It is also the negative slope of the force-displacement curve that can be drawn from Eq. (D19). The gravitational pull also puts an extra force on the SC sphere and displaces it from the origin along the negative $z$ axis. Then the total force on the SC sphere along the $z$ axis becomes $-\hat{k}(k_z\delta + m_{\mathrm{SC}}g)$, where $m_{\mathrm{SC}}$ and $g$ are the mass of the SC sphere and acceleration due to gravity. As a result, we can write the equilibrium position as $\delta_{\mathrm{eq}} \sim -m_{\mathrm{SC}}g/k_z$ If the slope of the force-displacement curve is not going to vary from the origin to the equilibrium position and also approximates the trap as a harmonic one, the angular frequency in radians of the trap along the $z$ axis at $\delta_{\mathrm{eq}}$ is given as $\omega_z = \sqrt{k_z/m_{\mathrm{SC}}}$.

To understand how much the demagnetizing field of the SC sphere affects the dipole magnetic field and the force due to it, we treat the presence of the SC sphere in the magnetic field as a perturbation and do not consider any change in the levitation magnetic fields due to demagnetization effects of the superconducting material of the SC sphere. To distinguish this case from the previous case, we denote the force, stiffness, equilibrium position, and trap frequency with an overline above the corresponding symbols.

The force on the particle along the $z$ axis is then [83,84]

$$\bar{\vec{F}}_{\mathrm{SC}} = \hat{k}\frac{\chi V}{\mu_0}B\frac{\partial B}{\partial z}, \tag{D20}$$

where $B = \sqrt{B_x^2+B_y^2+B_z^2}$, where $B_x$, $B_y$, and $B_z$ are the $x$, $y$, and $z$ components of the magnetic field. Since we are considering a perfect superconductor, we can consider $\chi \sim -1$. In contrast to the previous case, we consider $d_+ = d_-$. To obtain $B_x$, $B_y$, and $B_z$, we write $\Phi_{\mathrm{m}}$ directly in Cartesian

coordinates from Eq. (D1) as

$$\Phi_{\rm m}(x,y,z) = \frac{m}{4\pi}\left(\frac{(z-(d/2))}{(x^2+y^2+(z-(d/2))^2)^{3/2}} - \frac{(z+(d/2))}{(x^2+y^2+(z+(d/2))^2)^{3/2}}\right). \quad \text{(D21)}$$

Then we can write $B_x = -\mu_0 \partial \Phi_{\rm m}(x,0,0)/\partial x$, $B_y = -\mu_0 \partial \Phi_{\rm m}(0,y,0)/\partial y$, and $B_z = -\mu_0 \partial \Phi_{\rm m}(0,0,z)/\partial z$. $B_z$ is same as in Eq. (D13), as $d_+ = d_- = d/2$

Since we are interested in the force along the $z$ axis alone, where $x = y = 0$,

$$\vec{\bar{F}}_{\rm SC}(z) = -\hat{k}\frac{V}{\mu_0} B_{\rm m}(z)\frac{\partial B_{\rm m}(z)}{\partial z}. \quad \text{(D22)}$$

Then from Eq. (D18) using series expansion and considering only the first order, we get

$$\vec{\bar{F}}_{\rm SC} \sim -\hat{k}3072\frac{\mu_0 m^2}{\pi}\frac{\gamma^3}{d^8}\delta. \quad \text{(D23)}$$

Comparing Eqs. (D19) and (D23), we can see that the trap stiffness $k_z \sim 1.625\bar{k}_z$, the equilibrium position $\delta_{\rm eq} \sim \bar{\delta}_{\rm eq}/1.625$, and the trap frequency $\omega_z \sim 1.27\bar{\omega}_z$.

To validate this analytical method, we also built a COMSOL MULTIPHYSICS model with the same geometry as that in the above analysis (Fig. 9), except for magnetic spheres instead of magnetic dipoles. The magnetic field of a magnetic sphere with flux density $Br_{\rm magnet}$ and volume $V_{\rm magnet}$ is identical to that of a magnetic dipole with moment $m = \frac{1}{\mu_0} Br_{\rm magnet} V_{\rm magnet}$, so it will not affect the results. In the model, we took SC sphere radius $\gamma = 100$ μm, magnetic sphere radius $R_{\rm magnet} = 1000$ μm, distance between two magnets $d = 4000$ μm, and magnetic flux density $Br_{\rm magnet} = 1$ $T$. In the COMSOL MULTIPHYSICS simulation, the back-action of the demagnetizing field produced by the superconductor on the trapping magnetic fields is simulated well using COMSOL. We get the vertical trap stiffness $k_{z_\rm COMSOL} = 0.32$ N/m, which agrees well with $k_z = 0.34$ N/m from the analytical method involving the demagnetizing field using the same parameters. Considering $k_z \sim 1.625\bar{k}_z$, we can then conclude that the demagnetizing field of a superconductor in a trapping magnetic field is significant and it will change the vertical trap stiffness by 62.5% in this case.

## APPENDIX E: DECOHERENCE

In this appendix, we estimate the decoherence due to unavoidable noise (gas molecule collision, blackbody radiation, and magnetization fluctuation) and introduce measures to avoid other types of noise. We assume the proposals work in a vacuum with a pressure of approximately $10^{-16}$ mBar and a temperature of 10 mK. Note that these conditions are experimentally practical. A temperature of 10 mK is common for a dilution fridge. Because of the cryopumping effect, pressure even lower than $10^{-16}$ mBar has been easily reached at approximately 4 K in Penning traps [64,85]. We find in these conditions that gas molecule collision is the dominant damping source. We estimate the quality factor and the decoherence rate of the oscillators, which are dominated by gas molecule collision.

### 1. Gas molecule collision

#### *a. Q factor*

The $Q$ factor of a spherical oscillator due to gas molecule collision was worked out in Ref. [49]. We adapt it to estimate the $Q$ factors of our spherical YIG oscillator and flux qubit ring. We can write the $Q$ factor as [49]

$$Q_{\rm s} = 2\pi\frac{\text{Total energy stored}}{\text{Energy dissipated per cycle}} \approx 2\pi\frac{(1/2)M\omega_z^2 A_{\rm m}^2}{\bar{F}\times 4A_{\rm m}}, \quad \text{(E1)}$$

where $M$, $\omega_z$, and $A_{\rm m}$ are the mass, frequency (along the $z$ axis), and amplitude of the levitated objects, respectively. $\bar{F}$ is the average drag force on the levitated object (spherical magnet and flux qubit) due to gas collisions [49,63] Assuming that the average velocity (approximately $0.5\omega_z A_{\rm m}$) of the levitated object moving in the gas is much smaller than that of the surrounding gas molecules ($\sqrt{3k_{\rm B}T/M_{\rm g}}$), the average drag force can be written in a simplified form based on Refs. [49,63] as

$$\bar{F} \approx \frac{3}{2} C_{\rm d} A_{\rm c} P_{\rm g} \omega_z A_{\rm m}\sqrt{\frac{M_{\rm g}}{3k_{\rm B}T}}, \quad \text{(E2)}$$

where $A_{\rm c}$ is the cross-section area perpendicular to the direction of motion, $P_{\rm g}$ is the gas pressure, $M_{\rm g}$ is the mass of the gas molecule, which is assumed to be helium here, $k_{\rm B}$ is the Boltzmann constant, and $T$ is the temperature. The constant $C_{\rm d}$ is a constant depending on the shape of the levitated object. For a sphere, $C_{\rm d} = 4/3$ [63]. To calculate $C_{\rm d}$ for the ring, we consider that the ring with radius $R$ and cross-section radius $r$ can be approximated as a cylinder with radius $r$ and length $2\pi R$ when the ring moves in the direction perpendicular to the plane of the circle. For a cylinder, $C_{\rm d} = \pi/2$ [63]. Then from Eqs. (E1) and (E2), the $Q$ factor can be written as

$$Q = \frac{\pi}{6}\frac{\omega_z \rho}{P_{\rm g}}\sqrt{\frac{3k_{\rm B}T}{M_{\rm g}}}\left(\frac{V}{C_{\rm d}A_{\rm c}}\right), \quad \text{(E3)}$$

where $\rho$ and $V$ are the density and volume of the levitated object, respectively. For a spherical magnet, $A_{\rm c} = \pi r^2$, where $r$ in the case of sphere is the radius of the sphere,

and for a ring (cylinder), $A_c = 2r \times 2\pi R$. Then $V/C_d A_c$ for both the sphere and the ring is $r$. For the first scheme for levitating a spherical magnet, we estimate the $Q$ factor $Q_s$ of the 25 μm YIG sphere at 10 Hz as approximately $3.3 \times 10^{15}$. For the second scheme using an aluminum ring with $r = 5$ μm oscillating in the direction perpendicular to the ring plane at 10 Hz, the $Q$ factor $Q_r$ is estimated to be approximately $3.5 \times 10^{14}$.

#### *b. Decoherence rate*

The decoherence rate, which characterizes how long the oscillator's quantum motional state remains coherent, can be estimated from the $Q$ factors:

$$\Gamma_g = \gamma_g \frac{(\Delta z)^2}{\lambda_{dB}^2}, \tag{E4}$$

where $\gamma_g = \omega_z/Q$ is the damping rate, $\Delta z$ is the extent of superposition state separation, and $\lambda_{dB} = \hbar\sqrt{2\pi/M k_B T}$ is the de Broglie wavelength of the oscillator. As we noted in the main text, this scales quadratically with the size of the superposition $\Delta z$. Assuming $\Delta z = 1$ nm, we can estimate the decoherence rate $\Gamma_g$ for YIG to be 12 Hz, corresponding to a coherence time $1/\Gamma_g = 79$ ms. For the ring, we get the decoherence rate $\Gamma_g$ as 87 Hz with coherence time $1/\Gamma_g = 11$ ms. We will see the decoherence is dominated by gas molecule collision in our proposed schemes.

### 2. Blackbody radiation

We estimate the decoherence caused by blackbody radiation using the YIG sphere. The thermal de Broglie wavelength of massless particles is described by $\lambda_{BB} = \pi^{2/3}\hbar c/k_B T$ [86]. Under the proposed conditions, the thermal wavelength of blackbody radiation $\lambda_{BB} \sim 0.5$ m is much larger than the superposition separation $\Delta z$. Thus, the long-wavelength limit can be used to estimate the blackbody damping, and we obtain [86]

$$\Gamma_{BB} \approx \Lambda_{BB}(\Delta z)^2, \tag{E5}$$

where the decoherence parameters $\Lambda_{BB} = \Lambda_{BB,sc} + \Lambda_{BB,ab} + \Lambda_{BB,em}$, which consists of three contributions from scattering, absorption, and emission of thermal photons, are, respectively, given by

$$\Lambda_{BB,sc} = \frac{8! \times 8\zeta(9) c r^6}{9\pi} \left[\frac{k_B T_e}{\hbar c}\right]^9 \mathrm{Re}\left[\frac{\epsilon_{BB} - 1}{\epsilon_{BB} + 2}\right]^2, \tag{E6}$$

$$\Lambda_{BB,ab} = \frac{16\pi^5 c r^3}{189} \left[\frac{k_B T_e}{\hbar c}\right]^6 \mathrm{Im}\left[\frac{\epsilon_{BB} - 1}{\epsilon_{bb} + 2}\right], \tag{E7}$$

$$\Lambda_{BB,em} = \frac{16\pi^5 c r^3}{189} \left[\frac{k_B T_i}{\hbar c}\right]^6 \mathrm{Im}\left[\frac{\epsilon_{BB} - 1}{\epsilon_{BB} + 2}\right], \tag{E8}$$

where $\zeta(9)$ is the Riemann $\zeta$ function, $T_i$ is the bulk temperature of the oscillator, $T_e$ is the environment temperature, and $\epsilon_{BB}$ is the relative permittivity, which is assumed to be constant over the blackbody radiation. We take $T_i = T_e = 10$ mK and $\epsilon_{BB} = 12.5 + 2i$ [87], and then we estimate the decoherence rate $\Gamma_{BB}$ due to blackbody radiation for a sphere with radius $r = 25$ μm with superposition separation $\Delta z = 1$ nm to be $5 \times 10^{-28}$ Hz. The coherence time $1/\Gamma_{BB} = 2 \times 10^{27}$ s is huge, and thus the blackbody radiation can be ignored in our proposals.

### 3. Magnetization fluctuation

The fluctuation of magnetization of the magnets will also lead to decoherence of the system. The power spectrum of the magnetization fluctuation noise is given by [88]

$$S_M = \frac{1}{2\pi V} \frac{k_B T}{\omega_M} \mu''(\omega_M), \tag{E9}$$

where $V$ is the volume of the magnet and $\omega_M$ is the frequency and is considered as 1 Hz here. The magnet has a very low imaginary part of the permeability $\mu''(\omega_M)$ if it is fully saturated, and we consider $\mu''(\omega_M) = 3 \times 10^{-4}\mu_0$ [88]. The noise of the magnetic moment can be expressed as $\sqrt{S_m} = \sqrt{S_M} V$.

We first consider the decoherence due to the magnetization fluctuation of the YIG magnet. From Eq. (3) we know the magnetic field gradient at $z = 0$ generated by the flux qubits is given by

$$\frac{\partial B}{\partial z} = \frac{3\mu_0 I}{R^2} \frac{\eta}{(1 + \eta^2)^{5/2}}, \tag{E10}$$

where $I = 1000$ nA is the current circulating in the flux qubit, $R = 74$ μm is the radius of the flux qubit, and $\eta = z/R$ is a dimensionless factor describing the distance between flux qubits and the YIG magnet that maximizes the gradient field with $\eta = 0.5$. So the magnetic force noise on YIG can be expressed as

$$\sqrt{S_f^{mag}} = \frac{\partial B}{\partial z}\sqrt{S_m} = 1.4 \times 10^{-28}\ \mathrm{N}/\sqrt{\mathrm{Hz}}. \tag{E11}$$

We consider the force noise due to gas collisions, which is given by [73] $\sqrt{S_f^{gas}} = \sqrt{2k_B T M\gamma} = 1.3 \times 10^{-24}\ \mathrm{N}/\sqrt{\mathrm{Hz}}$.

The force noise due to magnetization fluctuation is much lower than the noise caused by gas collisions. Thus, it can be ignored for the decoherence consideration.

We now analyze the decoherence on the levitated flux qubit (ring) in the second scheme, caused by the magnetization fluctuation of the fixed permanent magnet. The

levitated ring above a permanent magnet with moment $m_{\rm mag}$ has the magnetic potential as [53]

$$E = \frac{\mu_0^2 m_{\rm mag}^2 R^4}{8L(z^2+R^2)^3}, \tag{E12}$$

where $R \approx 183$ μm is the radius of the flux qubit and $L = \mu_0 R[\ln(8R/r) - 2]$ is the self-inductance of the flux qubit, where $r$ is the radius of the cross section of the flux qubit. The magnetic force is thus given by

$$f_{\rm mag} = -\frac{\partial E}{\partial z} = \frac{3\mu_0^2 m_{\rm mag}^2 R^4 z}{4L(z^2+R^2)^4}. \tag{E13}$$

So the force noise due to magnetization fluctuation is expressed as

$$\sqrt{S_{\rm f}^{\rm mag}} = \frac{\partial f_{\rm mag}}{\partial m}\sqrt{S_{\rm m}} = 1.7 \times 10^{-25}\,{\rm N}/\sqrt{\rm Hz}. \tag{E14}$$

Considering the force noise due to gas collisions $\sqrt{S_{\rm f}^{\rm gas}} = \sqrt{2k_{\rm B}TM\gamma} = 3.5 \times 10^{-24}\,{\rm N}/\sqrt{\rm Hz}$, the noise due to magnetization fluctuation is much smaller, and can also be ignored for the levitated ring.

### 4. Interaction with a thermal phonon bath

The average phonon occupation number of a mechanical resonator can be written as $\bar{n} = 1/(e^{\frac{\hbar\omega_z}{k_{\rm B}T}} - 1)$. The motional thermal bath will interact with the motion of the resonator and change the phonon number. The phonon heating rate in the high-temperature limit is given by

$$\dot{\bar{n}} \approx \frac{k_{\rm B}T}{\hbar\omega_z}. \tag{E15}$$

At a bath temperature of $T = 10$ mK, we estimate the phonon heating rate as approximately $4.0 \times 10^{-7}$ Hz for the YIG magnet and approximately $3.7 \times 10^{-6}$ Hz for the ring.

### 5. External mechanical vibrations

The external vibrations are detrimental for superpositions of massive oscillators that possess small ground state

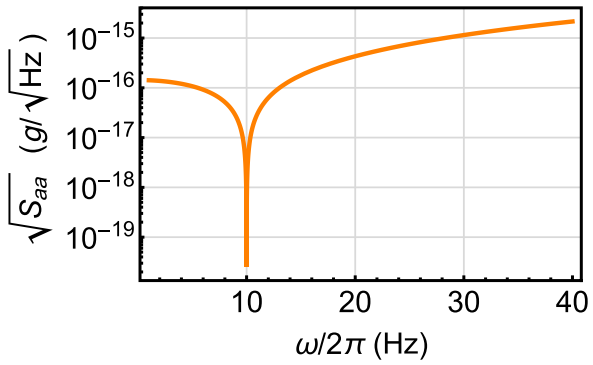



FIG. 10. Vibration acceleration level needed to keep the coherence time longer than 100 ms. Several methods should be used to isolate the vibration noise below that shown in the figure.

extensions. The decoherence caused by vibration noise can be estimated as $\Gamma_{\rm vib} \sim M^2\omega_z^4 S_{zz}\Delta_z^2/2\hbar^2$ [89], where $M$, $\omega_z$, and $S_{zz}$ are the mass, vertical frequency, and displacement noise power spectral density of the resonator, respectively. The acceleration, $a$, noise power spectral density can be written as $S_{aa} = S_{zz}((\omega_z^2 - \omega^2)^2 + (\gamma\omega)^2)$. In Fig. 10, we plot the vibration acceleration level that should be achieved to keep the coherence time longer than 100 ms. Any vibration source close to the resonance frequency (10 Hz) should be avoided. Seismic noise, which has low frequency and is one of the main vibration sources, should be suppressed to $\sqrt{S_{aa}} \leq 10^{-16}\, g/\sqrt{\rm Hz}$, where $g$ is the gravitational acceleration.

### 6. Coherence length

The quality of a macroscopic quantum superposition, particularly one that is subject to decoherence, can be quantified by more quantities that just the spatial separation of the superposition. The quantum coherence length $\ell$ provides a measure of the quality of the quantum superposition. Under decoherence, $\ell$ will decrease in time, but if this coherence length remains larger than the spatial separation of the superpositon $\ell > \Delta z$ over a reasonable time duration, then the superposition can be witnessed via the Ramsey sequence before the decoherence destroys the superposition. Our estimates of decoherence rates suggest that coherence can be maintained over the timescales relevant for superposition formation. We consider the

TABLE I. System parameters and the values used to introduce the first method.

| Quantity | Symbol | Value | Unit abbreviation |
|---|---|---|---|
| Density of YIG [90] | $\rho$ | 5110 | kg/m$^3$ |
| Remanent magnetic field of YIG [91] | $B_{\rm r}$ | $14.32 \times 10^{-3}$ | T |
| Magnitude of persistant current in the SC flux qubit | $I$ | 1000 | nA |
| Mass of the helium gas molecule | $M_{\rm g}$ | $6.65 \times 10^{-27}$ | kg |
| Boltzmann constant | $k_{\rm B}$ | $1.38 \times 10^{-23}$ | m$^2$ kg/K s$^2$ |

TABLE II. System parameters and the values used to introduce the second method.

| Quantity | Symbol | Value | Unit abbreviation |
|---|---|---|---|
| Radius of the magnetic sphere | $a$ | 12 | μm |
| Radius of the SC flux qubit | $R$ | 180–183.4 | μm |
| Radius of the cross-section of the SC flux qubit | $r$ | 5 | μm |
| Magnetic moment of the magnetic sphere | $m_{\mathrm{mag}}$ | $6.912 \times 10^{-9}$ | $\mathrm{A\,m^2}$ |
| Remanent flux density of the magnetic sphere | $Bz$ | 1.2 | T |
| Mass of the SC flux qubit | $M$ | $(2.41\text{–}2.45) \times 10^{-10}$ | kg |
| Self-inductance of the SC flux qubit | $L$ | $(8.28\text{–}8.48) \times 10^{-10}$ | H |
| Vacuum magnetic permeability | $\mu_0$ | $4\pi \times 10^{-7}$ | H/m |
| Magnetic flux quantum | $\Phi_0$ | $2.068 \times 10^{-15}$ | Wb |
| Superposition current in the SC flux qubit | $I$ | $\pm 1000$ | nA |
| Magnetic moment due to superposition current | $M_{\mathrm{SC}}$ | $(1.02\text{–}1.06) \times 10^{-13}$ | $\mathrm{A\,m^2}$ |
| Equilibrium position of the SC flux qubit | $h$ | 70–93 | μm |
| Vertical trap frequency | $\upsilon_z$ | 10–43 | Hz |
| Separation of superposition states | $\Delta z$ | 7–100 | nm |
| Zero-point motional extent | $\delta z_{\mathrm{ZPM}}$ | $6 \times 10^{-14}$ | m |
| Superposition separation in terms of $\delta z_{\mathrm{ZPM}}$ | $\chi$ | $2 \times 10^{6}$ | ... |

expression for the coherence length $\ell$ from Ref. [69] as

$$\ell(t) = \frac{1}{2}\left[\frac{3t^2 + 8\Lambda b^2 t^3 + 12M^2 b^4}{2\Lambda t^3 + 3M^2 b^2 + 4\Lambda^2 b^2 t^4 + 24\Lambda M^2 b^4 t}\right]^{1/2}, \tag{E16}$$

where $b = \Delta z$, $\Lambda = \gamma_{\mathrm{g}}/\lambda_{\mathrm{dB}}^2$ is the decoherence parameter, and $M$ is the mass. In the large-$t$ limit ($t$ is much larger than the localization timescale), the coherence length can be simplified as $\ell(t) \sim 1/\sqrt{2\Lambda t} = 1/\sqrt{2(\gamma_{\mathrm{g}}/\lambda_{\mathrm{dB}}^2)t}$. Assuming $\Delta z = 1$ nm and decoherence rate $\Gamma = \Lambda(\Delta z)^2 \sim 12$ Hz, we obtained $\ell(1\ \mathrm{ms}) \sim 9$ nm, indicating that the quality of the superposition will still be high up to $t = 1$ ms.

## APPENDIX F: TABLE OF VARIABLES AND THEIR VALUES CONSIDERED IN THE PRESENT STUDY

We list all the parameters and values used in Tables I and II.


[1] E. Schrödinger, Die gegenwärtige Situation in der Quantenmechanik, Naturwissenschaften **23**, 807 (1935).

[2] R. Penrose, On gravity's role in quantum state reduction, Gen. Relativ. Gravit. **28**, 581 (1996).

[3] A. Bassi, K. Lochan, S. Satin, T. P. Singh, and H. Ulbricht, Models of wave-function collapse, underlying theories, and experimental tests, Rev. Mod. Phys. **85**, 471 (2013).

[4] A. Vinante, R. Mezzena, P. Falferi, M. Carlesso, and A. Bassi, Improved noninterferometric test of collapse models using ultracold cantilevers, Phys. Rev. Lett. **119**, 110401 (2017).

[5] B. Helou, B. J. J. Slagmolen, D. E. McClelland, and Y. Chen, LISA pathfinder appreciably constrains collapse models, Phys. Rev. D **95**, 084054 (2017).

[6] D. Zheng, Y. Leng, X. Kong, R. Li, Z. Wang, X. Luo, J. Zhao, C.-K. Duan, P. Huang, J. Du, M. Carlesso, and A. Bassi, Room temperature test of the continuous spontaneous localization model using a levitated micro-oscillator, Phys. Rev. Res. **2**, 58 (2020).

[7] M. Rademacher, J. Millen, and Y. L. Li, Quantum sensing with nanoparticles for gravimetry: When bigger is better, Adv. Opt. Technol. **9**, 227 (2020).

[8] S. Bose, Matter wave Ramsey interferometry and the quantum nature of gravity, Available at https://www.youtube.com/watch?v=0Fv-0k13s_k (2016), Fundamental Problems of Quantum Physics, ICTS, Bangalore.

[9] S. Bose, A. Mazumdar, G. W. Morley, H. Ulbricht, M. Toroš, M. Paternostro, A. A. Geraci, P. F. Barker, M. S. Kim, and G. Milburn, Spin entanglement witness for quantum gravity, Phys. Rev. Lett. **119**, 240401 (2017).

[10] C. Marletto and V. Vedral, Gravitationally induced entanglement between two massive particles is sufficient evidence of quantum effects in gravity, Phys. Rev. Lett. **119**, 240042 (2017).

[11] G. Bhole, J. A. Jones, C. Marletto, and V. Vedral, Witnesses of non-classicality for simulated hybrid quantum systems, J. Phys. Commun. **4**, 025013 (2020).

[12] R. J. Marshman, A. Mazumdar, and S. Bose, Locality and entanglement in table-top testing of the quantum nature of linearized gravity, Phys. Rev. A **101**, 052110 (2020).

[13] M. Toroš, T. W. van de Kamp, R. J. Marshman, M. Kim, A. Mazumdar, and S. Bose, Relative acceleration noise mitigation for entangling masses via quantum gravity, Phys. Rev. Res. **3**, 023178 (2021).

[14] S. Bose, A. Mazumdar, M. Schut, and M. Toroš, Mechanism for the quantum natured gravitons to entangle masses, Phys. Rev. D **105**, 106028 (2022).

[15] N. Altamirano, P. Corona-Ugalde, R. B. Mann, and M. Zych, Gravity is not a pairwise local classical channel, Classical Quantum Gravity **35**, 145005 (2018).

[16] M. J. W. Hall and M. Reginatto, On two recent proposals for witnessing nonclassical gravity, J. Phys. A: Math. Theor. **51**, 085303 (2018).
[17] A. Belenchia, R. M. Wald, F. Giacomini, E. Castro-Ruiz, A. Brukner, and M. Aspelmeyer, Information content of the gravitational field of a quantum superposition, Int. J. Mod. Phys. D **28**, 1 (2019).
[18] M. Carlesso, A. Bassi, M. Paternostro, and H. Ulbricht, Testing the gravitational field generated by a quantum superposition, New J. Phys. **21**, 093052 (2019).
[19] M. Christodoulou and C. Rovelli, On the possibility of laboratory evidence for quantum superposition of geometries, Phys. Lett. Section B: Nucl. Elem. Part. High-Energy Phys. **792**, 64 (2019).
[20] H. C. Nguyen and F. Bernards, Entanglement dynamics of two mesoscopic objects with gravitational interaction, Eur. Phys. J. D **74**, 2 (2020).
[21] T. Krisnanda, G. Y. Tham, M. Paternostro, and T. Paterek, Observable quantum entanglement due to gravity, Npj Quantum Inf. **6**, 4 (2020).
[22] M. Arndt and K. Hornberger, Testing the limits of quantum mechanical superpositions, Nat. Phys. **10**, 271 (2014).
[23] Y. Y. Fein, P. Geyer, P. Zwick, F. Kiałka, S. Pedalino, M. Mayor, S. Gerlich, and M. Arndt, Quantum superposition of molecules beyond 25 kDa, Nat. Phys. **15**, 1242 (2019).
[24] M. Scala, M. Kim, G. Morley, P. Barker, and S. Bose, Matter-wave interferometry of a levitated thermal nano-oscillator induced and probed by a spin, Phys. Rev. Lett. **111**, 180403 (2013).
[25] C. Wan, M. Scala, G. Morley, A. A. Rahman, H. Ulbricht, J. Bateman, P. Barker, S. Bose, and M. Kim, Free nano-object Ramsey interferometry for large quantum superpositions, Phys. Rev. Lett. **117**, 143003 (2016).
[26] Y. Margalit, O. Dobkowski, Z. Zhou, O. Amit, Y. Japha, S. Moukouri, D. Rohrlich, A. Mazumdar, S. Bose, C. Henkel *et al.*, Realization of a complete Stern-Gerlach interferometer: Toward a test of quantum gravity, Sci. Adv. **7**, eabg2879 (2021).
[27] B. Wood, S. Bose, and G. Morley, Spin dynamical decoupling for generating macroscopic superpositions of a free-falling nanodiamond, Phys. Rev. A **105**, 012824 (2022).
[28] R. J. Marshman, A. Mazumdar, R. Folman, and S. Bose, Constructing nano-object quantum superpositions with a Stern-Gerlach interferometer, Phys. Rev. Res. **4**, 023087 (2022).
[29] R. Zhou, R. J. Marshman, S. Bose, and A. Mazumdar, Mass independent scheme for large spatial quantum superpositions, Phys. Rev. A **107**, 032212 (2023).
[30] S. Bose, K. Jacobs, and P. L. Knight, Preparation of nonclassical states in cavities with a moving mirror, Phys. Rev. A - At., Mol. Opt. Phys. **56**, 4175 (1997).
[31] Z.-q. Yin, T. Li, X. Zhang, and L. M. Duan, Large quantum superpositions of a levitated nanodiamond through spin-optomechanical coupling, Phys. Rev. A **88**, 033614 (2013).
[32] D. Lombardo and J. Twamley, Deterministic creation of macroscopic cat states, Sci. Rep. **5**, 13884 (2015).
[33] J.-Q. Liao and L. Tian, Macroscopic quantum superposition in cavity optomechanics, Phys. Rev. Lett. **116**, 163602 (2016).
[34] J. Clarke and M. R. Vanner, Growing macroscopic superposition states via cavity quantum optomechanics, Quantum Sci. Technol. **4**, 014003 (2018).
[35] H. Xie, X. Shang, C. G. Liao, Z. H. Chen, and X. M. Lin, Macroscopic superposition states of a mechanical oscillator in an optomechanical system with quadratic coupling, Phys. Rev. A **100**, 33803 (2019).
[36] L. Zheng, D. N. Chen, Z. Y. Peng, Y. Shi, Y. J. Liu, and Y. D. Wang, Macroscopic quantum superposition in optomechanical system with ultrastrong coupling light-matter interaction, Int. J. Theor. Phys. **59**, 824 (2020).
[37] I. Shomroni, L. Qiu, and T. J. Kippenberg, Optomechanical generation of a mechanical catlike state by phonon subtraction, Phys. Rev. A **101**, 033812 (2020).
[38] H. Zhan, G. Li, and H. Tan, Preparing macroscopic mechanical quantum superpositions via photon detection, Phys. Rev. A **101**, 063834 (2020).
[39] M. T. Johnsson, G. K. Brennen, and J. Twamley, Macroscopic superpositions and gravimetry with quantum magnetomechanics, Sci. Rep. **6**, 37495 (2016).
[40] O. Romero-Isart, Coherent inflation for large quantum superpositions of levitated microspheres, New J. Phys. **19**, 123029 (2017).
[41] A. T. M. A. Rahman, Large spatial Schrödinger cat state using a levitated ferrimagnetic nanoparticle, New J. Phys. **21**, 113011 (2019).
[42] W. Qin, A. Miranowicz, G. Long, J. Q. You, and F. Nori, Proposal to test quantum wave-particle superposition on massive mechanical resonators, Npj Quantum Inf. **5**, 58 (2019).
[43] J. S. Pedernales, G. W. Morley, and M. B. Plenio, Motional dynamical decoupling for interferometry with macroscopic particles, Phys. Rev. Lett. **125**, 23602 (2020).
[44] T. Kovachy, P. Asenbaum, C. Overstreet, C. A. Donnelly, S. M. Dickerson, A. Sugarbaker, J. M. Hogan, and M. A. Kasevich, Quantum superposition at the half-metre scale, Nature **528**, 530 (2015).
[45] L. Pezzè, M. Gessner, P. Feldmann, C. Klempt, L. Santos, and A. Smerzi, Heralded generation of macroscopic superposition states in a spinor Bose-Einstein condensate, Phys. Rev. Lett. **123**, 260403 (2019).
[46] M. Bild, M. Fadel, Y. Yang, U. von Lüpke, P. Martin, A. Bruno, and Y. Chu, Schrödinger cat states of a 16-microgram mechanical oscillator, Science **380**, 274 (2023).
[47] M. Cirio, G. K. Brennen, and J. Twamley, Quantum magnetomechanics: Ultrahigh-$Q$-levitated mechanical oscillators, Phys. Rev. Lett. **109**, 147206 (2012).
[48] M. T. Johnsson, G. K. Brennen, and J. Twamley, Macroscopic superpositions and gravimetry with quantum magnetomechanics, Sci. Rep. **6**, 37495 (2016).
[49] T. Wang, S. Lourette, S. R. O'Kelley, M. Kayci, Y. Band, D. F. J. Kimball, A. O. Sushkov, and D. Budker, Dynamics of a ferromagnetic particle levitated over a superconductor, Phys. Rev. Appl. **11**, 044041 (2019).
[50] J. Gieseler, A. Kabcenell, E. Rosenfeld, J. D. Schaefer, A. Safira, M. J. Schuetz, C. Gonzalez-Ballestero, C. C. Rusconi, O. Romero-Isart, and M. D. Lukin, Single-spin magnetomechanics with levitated micromagnets, Phys. Rev. Lett. **124**, 163604 (2020).

[51] M. Fuwa, R. Sakagami, and T. Tamegai, Ferromagnetic levitation and harmonic trapping of a milligram-scale yttrium iron garnet sphere, Phys. Rev. A **108**, 063511 (2023).

[52] R. Fitzpatrick, Uniformly magnetized sphere (2014), https://farside.ph.utexas.edu/teaching/jk1/Electromagnetism/node61.html Accessed: (2025-05-10).

[53] C. Navau, S. Minniberger, M. Trupke, and A. Sanchez, Levitation of superconducting microrings for quantum magnetomechanics, Phys. Rev. B **103**, 174436 (2021).

[54] C. Gonzalez-Ballestero, M. Aspelmeyer, L. Novotny, R. Quidant, and O. Romero-Isart, Levitodynamics: Levitation and control of microscopic objects in vacuum, Science **374**, 168 (2021).

[55] R. Metselaar and P. Larsen, Electrical properties of yttrium iron garnet, Proceedings of the International School of Physics Enrico Fermi **70**, 417 (1978).

[56] Y. Jin, K. Shen, P. Ju, and T. Li, Towards real-world applications of levitated optomechanics, ArXiv:2407.12496.

[57] K. Uhlig, Dry dilution refrigerator with pulse tube shutoff option, Cryogenics **130**, 103649 (2023).

[58] J. Franklin, J. Bedard, and I. Sochnikov, Versatile millikelvin hybrid cooling platform for superconductivity research, IEEE Trans. Appl. Supercond. **33**, 1 (2023).

[59] J. Hofer, R. Gross, G. Higgins, H. Huebl, O. F. Kieler, R. Kleiner, D. Koelle, P. Schmidt, J. A. Slater, M. Trupke, K. Uhl, T. Weimann, W. Wieczorek, and M. Aspelmeyer, High-$Q$ magnetic levitation and control of superconducting microspheres at millikelvin temperatures, Phys. Rev. Lett. **131**, 043603 (2023).

[60] Y. Leng, R. Li, X. Kong, H. Xie, D. Zheng, P. Yin, F. Xiong, T. Wu, C.-K. Duan, Y. Du *et al.*, Mechanical dissipation below 1 μHz with a cryogenic diamagnetic levitated microoscillator, Phys. Rev. Appl. **15**, 024061 (2021).

[61] C. Lee, H. Jo, C. S. Kang, G. B. Kim, I. Kim, Y. H. Kim, H. J. Lee, and J. So, Vibration mitigation for a cryogen-free dilution refrigerator for the AMoRE-pilot experiment, J. Low Temp. Phys. **193**, 786 (2018).

[62] B. van Heck, T. M. Fuchs, J. Plugge, W. A. Bosch, and T. H. Oosterkamp, Magnetic cooling and vibration isolation of a sub-kHz mechanical resonator, J. Low Temp. Phys. **210**, 588 (2023).

[63] B. De Lima Bernardo, F. Moraes, and A. Rosas, Drag force experienced by a body moving through a rarefied gas, Chin. J. Phys. **51**, 189 (2013).

[64] N. Hermanspahn, H. Häffner, H.-J. Kluge, W. Quint, S. Stahl, J. Verdú, and G. Werth, Observation of the continuous Stern-Gerlach effect on an electron bound in an atomic ion, Phys. Rev. Lett. **84**, 427 (2000).

[65] S. Caplan and G. Chanin, Critical-field study of superconducting aluminum, Phys. Rev. **138**, A1428 (1965).

[66] V. Kuznetsov and O. Trofimov, Critical temperatures and critical currents of wide and narrow quasi-one-dimensional superconducting aluminum structures in zero magnetic field, Physica C: Superconductivity and its Applications **595**, 1354030 (2022).

[67] F. Yan, S. Gustavsson, A. Kamal, J. Birenbaum, A. P. Sears, D. Hover, T. J. Gudmundsen, D. Rosenberg, G. Samach, S. Weber *et al.*, The flux qubit revisited to enhance coherence and reproducibility, Nat. Commun. **7**, 12964 (2016).

[68] L. V. Abdurakhimov, I. Mahboob, H. Toida, K. Kakuyanagi, and S. Saito, A long-lived capacitively shunted flux qubit embedded in a 3D cavity, Appl. Phys. Lett. **115**, 262601 (2019).

[69] D. Schlosshauer, *The Quantum-To-Classical Transition*, The Frontiers Collection (Springer-Verlag, Berlin, Germany, 2007).

[70] A. Somoroff, Q. Ficheux, R. A. Mencia, H. Xiong, R. Kuzmin, and V. E. Manucharyan, Millisecond coherence in a superconducting qubit, Phys. Rev. Lett. **130**, 267001 (2023).

[71] F. Wang, K. Lu, H. Zhan, L. Ma, F. Wu, H. Sun, H. Deng, Y. Bai, F. Bao, X. Chang *et al.*, High-coherence fluxonium qubits manufactured with a wafer-scale-uniformity process, Phys. Rev. Appl. **23**, 044064 (2025).

[72] L. Martinetz, K. Hornberger, J. Millen, M. Kim, and B. A. Stickler, Quantum electromechanics with levitated nanoparticles, Npj Quantum Inf. **6**, 101 (2020).

[73] M. Toroš, S. Bose, and P. Barker, Creating atom-nanoparticle quantum superpositions, Phys. Rev. Res. **3**, 033218 (2021).

[74] A. Vinante, A. Vinante, P. Falferi, G. Gasbarri, A. Setter, C. Timberlake, and H. Ulbricht, Ultralow mechanical damping with Meissner-levitated ferromagnetic microparticles, Phys. Rev. Appl. **13**, 064027 (2020).

[75] O. Chubar, P. Elleaume, and J. Chavanne, A three-dimensional magnetostatics computer code for insertion devices, J. Synchrotron Radiat. **5**, 481 (1998).

[76] B. F. Edwards, D. M. Riffe, J.-Y. Ji, and W. A. Booth, Interactions between uniformly magnetized spheres, Am. J. Phys. **85**, 130 (2017).

[77] O. Romero-Isart, L. Clemente, C. Navau, A. Sanchez, and J. I. Cirac, Quantum magnetomechanics with levitating superconducting microspheres, Phys. Rev. Lett. **109**, 147205 (2012).

[78] J. Hofer and M. Aspelmeyer, Analytic solutions to the Maxwell–London equations and levitation force for a superconducting sphere in a quadrupole field, Phys. Scr. **94**, 125508 (2019).

[79] M. W. Coffey, Levitation force between a point magnetic dipole and superconducting sphere, J. Supercond. Novel Magn. **13**, 381 (2000).

[80] Q.-G. Lin, Analytic solutions to Maxwell–London equations and levitation force for a general magnetic source in the presence of a long type-II superconducting cylinder, The European Physical Journal B **54**, 27 (2006).

[81] J. L. Perez-Diaz and J. C. Garcia-Prada, Interpretation of the method of images in estimating superconducting levitation, Physica C: Superconductivity and its Applications **467**, 141 (2007).

[82] M. W. Coffey, London model for the levitation force between a horizontally oriented point magnetic dipole and superconducting sphere, Phys. Rev. B **65**, 214524 (2002).

[83] M. C. O'Brien, S. Dunn, J. E. Downes, and J. Twamley, Magneto-mechanical trapping of micro-diamonds at low pressures, Appl. Phys. Lett. **114**, 053103 (2019).

[84] J. P. Houlton, M. L. Chen, M. D. Brubaker, K. A. Bertness, and C. T. Rogers, Axisymmetric scalable magneto-gravitational trap for diamagnetic particle levitation, Rev. Sci. Instrum. **89**, 125107 (2018).

[85] G. Gabrielse, Antiproton mass measurements, Int. J. Mass Spectrom. **251**, 273 (2006).

[86] O. Romero-Isart, Quantum superposition of massive objects and collapse models, Phys. Rev. A **84**, 052121 (2011).

[87] A. Sharma, I. Mohammed, S. K. Godara, and A. K. Srivastava, Low dielectric losses and enhanced magnetic property of ErIG(x)/YIG(1- x)(x = 0.5) composite for antenna applications, Bull. Mater. Sci. **45**, 248 (2022).

[88] I. Bloch, D. Budker, V. Flambaum, I. Samsonov, A. Sushkov, and O. Tretiak, Scalar dark matter induced oscillation of a permanent-magnet field, Phys. Rev. D **107**, 075033 (2023).

[89] O. Romero-Isart, Coherent inflation for large quantum superpositions of levitated microspheres, New J. Phys. **19**, 123029 (2017).

[90] T. Seberson, P. Ju, J. Ahn, J. Bang, T. Li, and F. Robicheaux, Simulation of sympathetic cooling an optically levitated magnetic nanoparticle via coupling to a cold atomic gas, J. Opt. Soc. Am. B **37**, 3714 (2020).

[91] M. A. Musa, R. S. Azis, N. H. Osman, J. Hassan, and T. Zangina, Structural and magnetic properties of yttrium iron garnet (YIG) and yttrium aluminum iron garnet (YAlG) nanoferrite via sol-gel synthesis, Results Phys. **7**, 1135 (2017).